Journal of Applied Physics

RESEARCH ARTICLE | FEBRUARY 04 2025

# Perturbation energy extraction from a fluid via a subsurface acoustic diode with sustained downstream attenuation

R. Schmidt ; H. Yousef ; I. Roy ; C. Scalo ; M. Nouh



*J. Appl. Phys.* 137, 054901 (2025)
https://doi.org/10.1063/5.0226396



AIP Publishing

Journal of Applied Physics ARTICLE pubs.aip.org/aip/jap

# Perturbation energy extraction from a fluid via a subsurface acoustic diode with sustained downstream attenuation

Cite as: J. Appl. Phys. **137**, 054901 (2025); doi: 10.1063/5.0226396
Submitted: 1 July 2024 · Accepted: 7 January 2025 ·
Published Online: 4 February 2025



R. Schmidt,[1] H. Yousef,[1] I. Roy,[2] C. Scalo,[2,3] and M. Nouh[1,4,a)]

## AFFILIATIONS

[1]Department of Mechanical and Aerospace Engineering, University at Buffalo (SUNY), Buffalo, New York 14260-4400, USA
[2]School of Mechanical Engineering, Purdue University, West Lafayette, Indiana 47907-2088, USA
[3]School of Aeronautics and Astronautics, Purdue University, West Lafayette, Indiana 47907-2045, USA
[4]Department of Civil, Structural and Environmental Engineering, University at Buffalo (SUNY), Buffalo, New York 14260-4300, USA

[a)]**Author to whom correspondence should be addressed:** mnouh@buffalo.edu

## ABSTRACT

Engineered subsurface structures inspired by phononic materials have shown favorable capabilities in flow control. Current efforts rely on tuning a structural resonance to the frequency of an unstable fluid mode, causing the deformations of the interfacing solid to destructively interfere with a wave-like flow instability. Although promising, the technique is most effective at targeting a single frequency mode with high-Q resonance. Additionally, several studies have shown the reduction in the perturbation energy to be spatially localized to the flow region above the subsurface strip, with a severely worsening effect downstream. Motivated by a desire to overcome these limitations, we present a different approach to methodically extract an undesirable pressure disturbance from a fluid column in a manner that capitalizes on the broad frequency range of a phononic bandgap, with the goal of permanently confining the perturbation energy within the subsurface structure. An acoustic diode (AD), i.e., a unidirectional transmitter of mechanical energy, comprised of a bi-layered phononic crystal and an auxiliary medium, interacts with a fluid cavity and provides a terminal energy sink. Two distinct ADs are presented that demonstrate active (time-variant) and passive (strain-dependent) paths to concept realization. The AD's performance is described in terms of the time-transient energy distribution in the fluid and the interacting structure, as well as spatial wave profiles at critical time instants. The results show the system's ability to achieve robust extraction of undesirable fluid oscillations with minimal residual energy. The concept is then tested in a fully developed plane channel flow with a superimposed perturbation, demonstrating the sustained nature of the subsurface AD's energy trapping mechanism in addition to its ability to induce downstream attenuation.





## I. INTRODUCTION

The interaction of a fluid with a deformable solid is a complex problem at the nexus of fluid and structural mechanics. Their implications represent a key consideration in many applications across varying size scales, from turbines and aircraft wings[1,2] down to blood vessels.[3] The problem is also central to the laminar-to-turbulent flow transition in a fluid as a result of rapidly growing perturbations such as Tollmien–Schlichting (TS) waves or vortical disturbances.[4,5] Owing to the increased skin friction drag associated with such transition, and the consequent rise in fuel consumption, there is a long-standing interest in novel techniques that delay boundary layer transition in aero/hydrodynamic flows. Disturbances arising in a wall-bounded flow involve a well-established dependency on wall parameters such as geometry, compliance, and surface roughness.[6,7] By understanding the role of these parameters in shaping the fluid response, the conditions that breed these perturbations can be reversed through *prescribed* fluid–wall interactions. The use of riblets for viscous drag reduction has been one of the most researched topics,[8] with numerical[9] and experimental[10] investigations of various swept wings and airfoils. Parallel efforts include the use of bio-inspired surfaces,[11]

hydrophobic microgrooves,[12,13] and compliant coatings.[14,15] Stabilization of fluid disturbances through wave cancelation techniques have also been investigated for decades. Owing to their wave-like nature, these methods have shown promise in inhibiting the growth of some perturbations associated with flow transition. Aside from Helmholtz resonators,[16,17] the majority of these efforts involve active interventions in the form of targeted destructive interferences at wavelengths and frequencies of interest.[18–23] Maintenance cost and the added complexity of integrating (and tuning) a controller have spurred the need for passive approaches, which perform at par with their active counterparts.

Over the past two decades, architected materials have evolved from fanciful ideas to realistic designs which alter the structural response in unprecedented ways. The interactions between a fluid and a metamaterial have since been repeatedly studied.[24–27] Motivated by this, the seminal work of Hussein *et al.* in 2015 showed that the elastic deformation profile of a subsurface phononic crystal (PnC) can passively stabilize a fluid, effectively reducing the average perturbation energy production rate.[28] In this context, a structural resonance placed within the PnC bandgap (BG) (also known as a truncation resonance[29,30]) provides favorable phase conditions and enables the subsurface's deformations to counter the fluid's velocity causing the growing wave to attenuate. The idea provided an analogous technique to that proposed by Milling in the early 1980s,[31] albeit critically without the need for active wave generators. Many variations of this concept has since followed,[32,33] and while the initial analysis used water, there has been an influx of research efforts which have taken a closer look at the use of subsurface phononic materials for transition delay in low-speed aerodynamic flows.[34–37]

As compelling as the concept is, ensuing investigations showed a number of limitations, which can be summarized as follows: (1) The approach relies predominantly on a truncation resonance which takes place at a single frequency. As is the case with any resonant behavior, the drop in deformation amplitude renders the technique ineffective outside this resonance since the method requires the solid to sufficiently deform to produce discernible wave cancelation. (2) The working mechanism requires high-amplitude deformations and certain phase conditions. Both are criteria that can be provided by traditional resonances, without the need for a bandgap, thus eliminating the need for PnCs. In fact, a more recent investigation by Kianfar and Hussein demonstrated that the same effect can be reproduced by a conventional passband (PB) resonance which precedes the bandgap.[38] (3) The stabilization effect has been consistently shown to be short lived. Specifically, the fluid perturbation has been shown to re-grow downstream of the subsurface PnC with a rapid energy recovery rate. The use of multiple PnCs over extended spatial domains (which raises practical considerations) has been shown to push this recovery further downstream, but not prevent it from happening.[39,40] Others have devised different strategies to eliminate the same adverse effect by employing a subsurface PnC which interfaces with the fluid at two distinct, spaced-out locations, effectively injecting energy into the fluid upstream while extracting energy from it downstream.[41]

In this work, we propose a different approach to methodically extract energy from an oscillating fluid and retain the energy in a subsurface structure which acts as a permanent energy sink. We utilize the notion of an acoustic diode, i.e., a unidirectional transmitter of mechanical energy (first introduced by Liang *et al.*[42]), to form the basis of a subsurface structure which directly interfaces with a fluid column subject to pressure oscillations, with the goal of fully absorbing them. In doing so, we demonstrate a tunable technique which enables energy extraction from a fluid over a wider range of frequencies or targeting a mode with a broad resonance peak, consistent, for example, with the realistic spectrum of a TS wave in transonic regimes, by effectively utilizing the entire frequency range of a Bragg bandgap as the subsurface structure's operational range. To elucidate the analysis, we first pose the problem in the form of a one-dimensional channel which comprises a slender fluid cavity coupled to a multi-layered structure, which in itself consists of a bi-layered PnC and an auxiliary medium that serves as a terminal energy sink. We start by synthesizing the auxiliary segment from a time-varying material (TVM) to illustrate the energy extraction potential of the subsurface diode in its idealized form. However, to maintain its passive nature, we then shift to two different nonlinear material models, seeking to achieve the same behavior in a time-invariant medium through different strain dependencies. To interpret the nuanced interactions between each two successive layers in the overall system, the performance is shown in terms of the time-transient energy distribution in the fluid and the interacting solid, as well as spatial snapshots at relevant time instants. The fluid–structural interactions are also captured via a time-domain impedance boundary condition (TDIBC) approach, which confirms the finite element model predictions. Following the proof-of-concept one-dimensional problem, we conclude by demonstrating the ability of the subsurface AD to attenuate the perturbation energy contained within a two-dimensional, fully developed channel flow across both time (sustained attenuation) and space (non-localized, downstream attenuation). The combined analytical–numerical framework presented here provides a pathway for efficient extraction of a perturbation from an oscillating fluid using a fine-needle approach, which leaves minimal residual energy and eliminates the prospect of perturbation recovery in the fluid medium.



## II. LF–PnC INTERACTION IN THE ABSENCE OF AN ENERGY TRAP

### A. PnC characterization

We start by quantifying the wave propagation characteristics of the phononic crystal (PnC), to be later placed beneath a linear fluid (LF) column subject to undesirable pressure oscillations at a target frequency. The PnC, depicted in Fig. 1(a), takes the form of a one-dimensional rod (i.e., elastic bar) which is comprised of two alternating materials of length $L_i$, cross-sectional area $A_i$, density $\rho_i$, and elastic modulus $E_i$, where $i = 1, 2$. Table I lists the physical and geometrical parameters used for both layers. The transfer matrix method (TMM) is employed to generate the dispersion diagram of the PnC [see Eq. (7) and Refs. 43–46]. The dispersion relation of an infinitely long PnC is obtained from the transfer

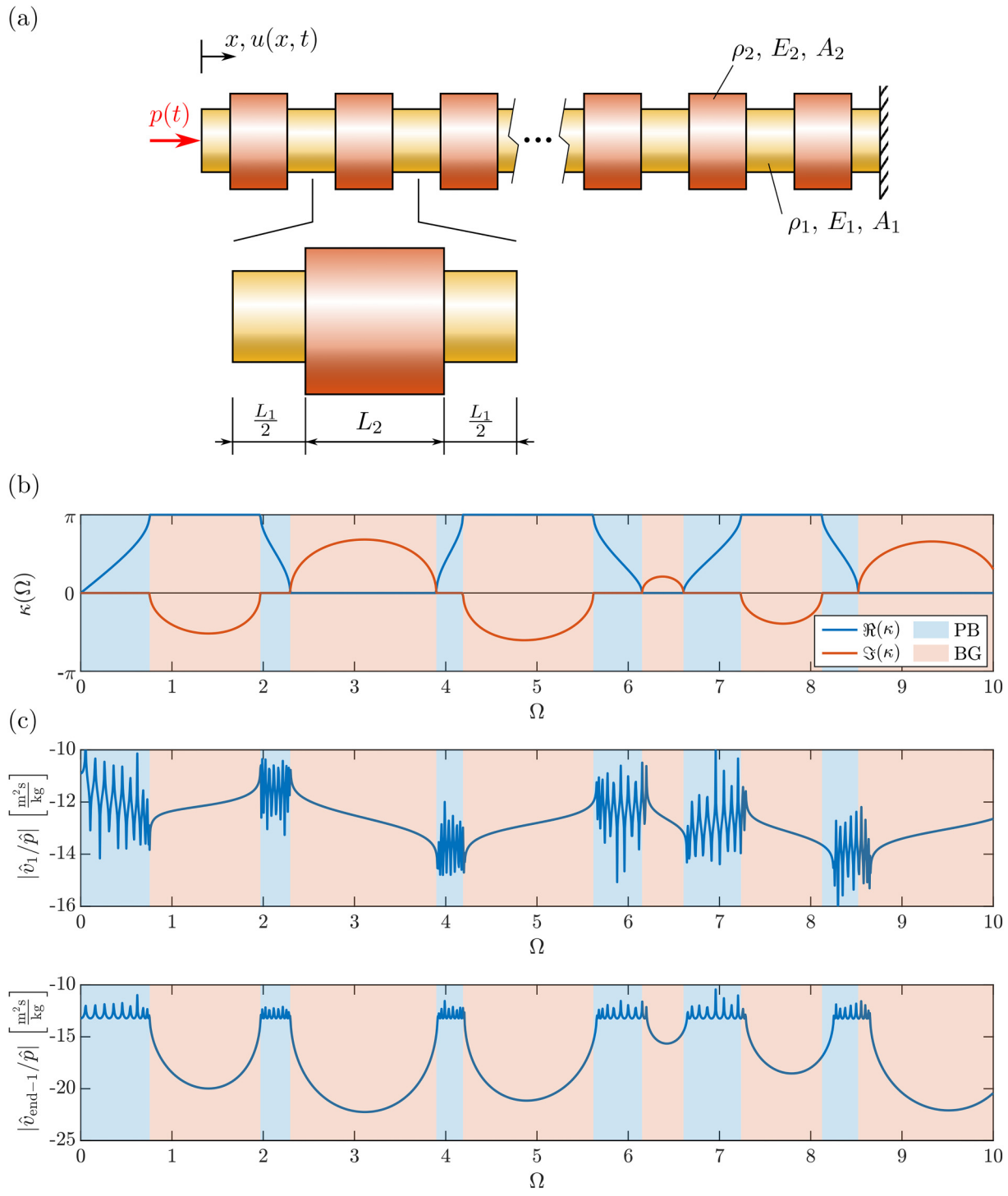


**FIG. 1.** Characterization of the phononic crystal (PnC). (a) Schematic diagram of a free-fixed finite PnC rod comprising a one-dimensional periodic array of 10 unit cells. Close up shows an individual unit cell comprising two alternating layers ($i = 1, 2$). (b) Dispersion diagram of the shown unit cell corresponding to the geometric and material properties listed in Table I. (c) Frequency response functions (FRFs) of the first and last (non-fixed) finite element node of the free-fixed PnC in response to an impinging pressure at the free end. Color-coded shaded regions indicate pass band (PB) and bandgap (BG) frequency ranges in (b) and (c).

**TABLE I.** Properties and geometrical parameters for the linear fluid (LF) column, the two phononic crystal (PnC) layers, and different forms of the augmenting layer attached to the PnC.

| | | PnC | | | |
|---|---|---|---|---|---|
| | LF | $(i=1)$ | $(i=2)$ | LM/TVM[a]/NLM[a] | Units |
| $\rho_i$ | 1870 | 1040 | 2700 | 1870 | $\frac{\text{kg}}{\text{m}^3}$ |
| $A_i$ | 25 | 25 | 25 | 25 | $\text{mm}^2$ |
| $E_i$ | 3.57 | 2.4 | 69 | 3.57 | GPa |
| $L_i$ | 87 | 2.9 | 2.9 | 87 | mm |
| $z_i$ | 64.59 | 39.50 | 341.23 | 64.59 | $\frac{\text{N s}}{\text{m}}$ |
| $\omega_i$ | … | $524\times10^3$ | $174\times10^4$ | … | rad/s |

[a]Given value for the elastic modulus of the TVM and NLM (both NLM-A/NLM-B) holds only for the initial undeformed state.

matrix of the self-repeating unit cell and is described by[29]

$$\kappa = \cos^{-1}\left[\frac{\cos(2\Omega) - \beta^2\cos(2\alpha\Omega)}{1-\beta^2}\right], \tag{1}$$

where $\kappa$ and $\Omega = \omega/\omega_0$ represent the nondimensional wavenumber and frequency of a propagating wave, respectively. The latter is expressed as a function of the angular frequency of excitation $\omega$ and the harmonic angular mean frequency $\omega_0$, given by

$$\omega_0 = \frac{2\omega_1\omega_2}{\omega_1+\omega_2}, \tag{2}$$

where $\omega_i = \sqrt{E_i/(\rho_i L_i^2)}$. Finally, in Eq. (1), the nondimensional values $\alpha$ and $\beta$ denote the frequency and impedance contrasts given by

$$\alpha = \frac{\omega_2-\omega_1}{\omega_1+\omega_2}, \tag{3a}$$

$$\beta = \frac{z_1-z_2}{z_1+z_2}, \tag{3b}$$

where the impedance $z_i$ of each PnC layer is given by $z_i = A_i\sqrt{E_i\rho_i}$. Figure 1(b) shows the dispersion diagram of the PnC, presenting the frequency-dependence of both the real and imaginary components of the nondimensional wavenumber, $\Re(\kappa)$ and $\Im(\kappa)$, respectively. A bandgap (BG), i.e., a frequency range of forbidden wave propagation, emerges in the regions corresponding to a non-zero value of $\Im(\kappa)$ due to Bragg scattering, and the magnitude of $\Im(\kappa)$ indicates the strength of the wave's spatial attenuation inside the PnC at a given BG frequency. Impinging waves are able to freely transmit through the PnC outside of the BG ranges and are lossless in both space and time due to the lack of material damping. These transmission ranges denote the PnC's passbands (PBs). Table II lists the lower and upper frequency bounds of the PnC's first two PBs and BGs, which will be referenced in the coming sections.

**TABLE II.** Lower and upper bandgap (BG) bounds corresponding to the infinite PnC shown in Fig. 1.

| | | First BG | Second BG |
|---|---|---|---|
| Start | $\Omega$ | 0.7554 | 2.2962 |
| | $\omega/2\pi$ (kHz) | 96.9 | 294.4 |
| End | $\Omega$ | 1.9693 | 3.8971 |
| | $\omega/2\pi$ (kHz) | 252.5 | 499.7 |

Finally, to characterize the vibrational response of a finite periodic realization of the PnC, two frequency response functions (FRFs) of a free-fixed PnC consisting of 10 unit cells are depicted in Fig. 1(c). The rod's elastic deformation and velocity are described by the continuous functions $u(x,t)$ and $v(x,t) = \partial u/\partial t$ of the Lagrangian coordinate $x$ and time $t$, subject to the harmonic pressure excitation $p(t) = \hat{p}\sin(\Omega t)$, where $\hat{p}$ is the pressure amplitude, applied at the rod's free end, as shown in Fig. 1(a). The rod is discretized into 30 two-node bar elements per unit cell (300 elements in total) and FRFs are computed for the first and second-to-last nodes as a ratio of the impinging pressure, i.e., $|\hat{v}_1/\hat{p}|$ and $|\hat{v}_{\text{end}-1}/\hat{p}|$, using a finite element model (FEM). The former FRF exhibits a series of resonances and anti-resonances sandwiched between one another within the rod's PBs (typical of a collocated sensor–actuator problem), while the latter FRF only shows the resonant frequencies at the same locations. As predicted by the dispersion analysis, both FRFs confirm the lack of transmission within BGs and a significant spatial decay of the wave's amplitude along the length of the PnC, as evident by $|\hat{v}_{\text{end}-1}/\hat{p}|$ within BG areas. Slight discrepancies between the predicted BG ranges and the amplitude drops in the FRFs can be seen at higher frequencies, which is typical of any FEM and can be minimized with a finer mesh.

## B. Energy exchange between LF and PnC

Upon identifying the PnC's propagating and attenuating regions, we examine the interaction and energy flow from a linear fluid column (henceforth referred to as LF) to a PnC of 10 unit cells and the same parameters listed in Table I, connected in series from one end to the fluid and fixed at the opposite end, as depicted in Fig. 2(a). A pressure wave in the form of a narrowband Gaussian wave pulse excites the fluid at $x = -L_{\text{LF}}$ as shown in the figure and is described by

$$p(t) = \hat{p}\, e^{\frac{-1}{2\sigma}(t-\bar{t})^2}\cos[2\pi f_c(t-\bar{t})], \tag{4}$$

where $\hat{p} = 1$ Pa denotes the maximum pressure amplitude, $\sigma = 2.8\times10^{-10}\,\text{s}^2$ the time compression factor, $f_c$ is the central frequency of the wave packet, and $\bar{t} = 7.1\times10^{-5}$ s represents the time instant at which the pressure pulse reaches its maximum amplitude. Two separate pulses, with frequencies of $f_c = 70$ kHz and $f_c = 140$, are used to excite the LF–PnC system to investigate the energy transmission profiles when the dominant frequency of the oscillating pressure in the fluid lies outside and inside the PnC's BG, respectively (see the supplementary material Movie 1).

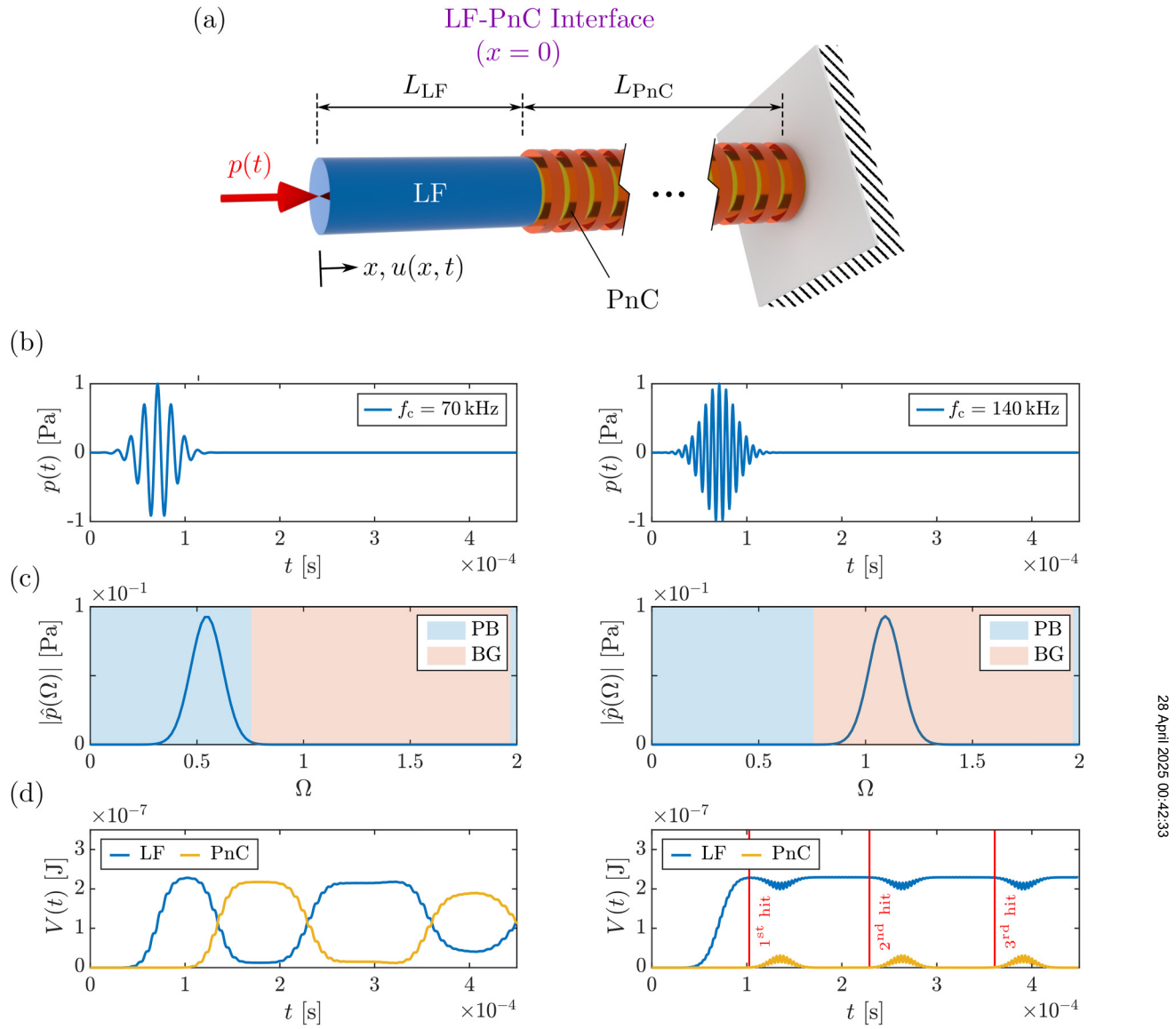


**FIG. 2.** Energy exchange between LF and PnC. (a) Schematic diagram of a linear fluid (LF) column interfacing with a one-dimensional PnC rod comprising 10 unit cells. The LF–PnC interface is denoted as the $x = 0$ point and the PnC is fixed at $x = L_{PnC}$. The LF is excited at the far left end ($x = -L_{LF}$) with a pressure pulse $p(t)$. (b) Variation with time of $p(t)$ with a central frequency of $f_c = 70$ kHz (left) and $f_c = 140$ kHz (right). (c) Fourier transform of $p(t)$ showing the frequency spectrum $|\hat{p}(\Omega)|$ as a function of the normalized frequency $\Omega$, showing that the first pressure pulse falls outside the PnC's BG while the second one falls inside it. (d) Energies contained within the two segments, LF and PnC, at any given time instant throughout the simulated interval. The left-hand side temporal energy profile shows the bulk energy being transferred back and forth between the two media when $f_c = 70$ kHz, as a result of the PnC admitting the incident wave from the fluid side. The right-hand side temporal profile shows the energy impinging on the PnC being predominantly rejected and forced to stay within the fluid column for the duration of the simulation, $f_c = 140$ kHz which represents a BG frequency.

$x = 0$ represents the LF–PnC interface. Figures 2(b) and 2(c) show the time signal and frequency spectra of both excitations, respectively. The incident pressure wave travels through the fluid column until it reaches the LF–PnC interface. For the case when $f_c = 70$ kHz, the wave is transmitted freely from the LF to the PnC since it falls within a pass band frequency (barring some reflections due to the impedance mismatch at the LF–PnC interface), and propagates through the elastic structure until it reaches the PnC's fixed end. At which point, the wave bounces back off of the rigid termination through the PnC and back into the LF. This process

repeats itself in a cyclic manner and is captured in the left panel of Fig. 2(d) which shows the energies stored in each layer, LF and PnC, over a time interval of 0.45 ms. The system's total energy $V_{\text{tot}} = V_{\text{LF}} + V_{\text{PnC}}$ is given by

$$V_{\text{LF}} = \frac{\rho_{\text{LF}} A_{\text{LF}}}{2} \int_{L_{\text{LF}}} u_{,t}^2 \, dx + \frac{E_{\text{LF}} A_{\text{LF}}}{2} \int_{L_{\text{LF}}} u_{,x}^2 \, dx \tag{5}$$

and

$$V_{\text{PnC}} = \sum_{n=1}^{10} \left[ \sum_{i=1}^{2} \left( \frac{\rho_i A_i}{2} \int_{L_i} u_{,t}^2 \, dx + \frac{E_i A_i}{2} \int_{L_i} u_{,x}^2 \, dx \right) \right], \tag{6}$$

where $i = 1, 2$ denote the two materials of the bi-layered PnC, $n = 1, 2, \ldots, 10$ indicates the unit cell index within the PnC, and the notations $(\ldots)_{,t}$ and $(\ldots)_{,x}$ denote partial differentiations with respect to $t$ and $x$, respectively. The energy distribution over time is computed via transient FEM simulations using MATLAB's built-in ode45 function. Vertical lines indicate the time instants at which the pressure wavefront hits the LF–PnC interface, and the noticeable reduction in the energy curves for each medium from one cycle to the next signifies the reflections at the interface. For the case when $f_c = 140$ kHz, the impinging pressure wave lies squarely within the PnC's first BG (see Table II), and therefore travels through the fluid and is predominantly rejected at the LF–PnC interface. As a result, the bulk portion of the energy remains confined within the LF throughout the simulation, as confirmed by the shown curves. Minor bumps in the energy stored within the PnC indicate the small amount of energy which transmits from the LF each time the wave arrives at the interface and spatially attenuates along the length of the PnC due to the BG-induced Bragg scattering.[29] Both pressure signals show that the PnC is unable to solely extract undesirable oscillations from an adjacent fluid at a target frequency, regardless of whether the incident excitation falls outside or inside its BGs, motivating the need for an energy trap mechanism which augments the subsurface PnC, as will be detailed in Sec. III.

### C. Validation via time-domain impedance boundary condition approach

An impedance boundary condition (IBC) at the LF–PnC interface can be alternatively used to model the subsurface PnC, as shown in Fig. 3(b). The effective impedance seen by the fluid at the LF–PnC interface due to the presence of the PnC can be given by the transfer matrix method (TMM). The transfer matrix of the 10-cell PnC is

$$\mathbf{T}_{\text{PnC}} = (\mathbf{T}_2 \mathbf{T}_1)^{10}, \quad \mathbf{T}_i = \begin{bmatrix} \cos\left(\frac{\omega L_i}{c_i}\right) & j\rho_i c_i \sin\left(\frac{\omega L_i}{c_i}\right) \\ \frac{j}{\rho_i c_i} \sin\left(\frac{\omega L_i}{c_i}\right) & \cos\left(\frac{\omega L_i}{c_i}\right) \end{bmatrix}, \tag{7}$$

where $i = 1, 2$ denotes the two materials of the bi-layered PnC, $j = \sqrt{-1}$, and $c_i = \sqrt{E_i/\rho_i}$ is the wave speed in each PnC layer. Imposing the hard wall constraint at $x = L_{\text{PnC}}$ by forcing the velocity fluctuations $\hat{v}_{L_{\text{PnC}}} = 0$, the effective specific impedance (i.e., impedance over cross-sectional area) at the LF–PnC interface can be obtained as

$$\hat{Z}(\omega) = -j\rho_{\text{eff}} c_{\text{eff}} \cot\left(\frac{\omega L_{\text{PnC}}}{c_{\text{eff}}}\right) = \frac{\hat{p}_0(\omega)}{\hat{v}_0(\omega) \cdot \mathbf{n}}, \tag{8}$$

where $\rho_{\text{eff}}$ and $c_{\text{eff}}$ are effective parameters of the transfer matrix of the PnC system $\mathbf{T}_{\text{PnC}}$, which has a similar mathematical form as $\mathbf{T}_i$ in Eq. (7). $\hat{p}_0$ and $\hat{v}_0$ are the Fourier transforms of pressure and velocity fluctuations at the interface ($x = 0$), and $\mathbf{n}$ denotes the unit normal vector pointing away from the LF into the PnC. Note that the impedance obtained using the TMM assumes linear propagation dynamics within the PnC and at the LF–PnC interface.

The compressible Navier–Stokes equations are solved to simulate the propagation dynamics of the imposed acoustic wave given by Eq. (4) in the LF domain. The simulations are performed using CFDSU,[47] a Fortran-based finite differencing solver that is continuously being developed at Purdue University and has been used previously for various types of flow applications.[48,49] The complex impedance at the LF–PnC interface is imposed as a time-domain impedance boundary condition (TDIBC). This constitutes imposing a time-domain equivalent of Eq. (8), which takes the form of a convolution integral that is to be solved numerically. Several constraints are required to be satisfied to enforce a physically meaningful and numerically stable TDIBC, which are summarized by Douasbin *et al.*[50] and Chen and Scalo.[51] The TDIBC implementation in CFDSU accounts for these constraints and adopts the auxiliary differential equation (ADE) method, originally proposed by Dragna *et al.*[52] The ADE method translates the convolution integral to a set of ODEs for two auxiliary variables that can be advanced in time with the same time marching technique as the flow solver.

The TDIBC does not directly impose the complex impedance $\hat{Z}(\omega)$ but rather translates it to obtain a complex wall softness coefficient $\hat{S}(\omega) = 2/(1 + \hat{Z}(\omega))$.[53] Imposing the wall softness avoids singularity issues as the absolute value of the complex impedance may range from $[0, \infty)$. The wall softness further relates the acoustic characteristic wave leaving the domain, $\hat{v}_n^{\text{out}}(\omega)$ and the characteristic wave entering the domain after interaction with the impedance surface, $\hat{v}_n^{\text{in}}(\omega)$. The aim of the TDIBC method is to obtain the wave reflected back from the impedance surface ($\hat{v}_n^{\text{in}}$) for a given incoming wave ($\hat{v}_n^{\text{out}}$). This relation in the time domain translates to

$$\begin{aligned} &\hat{v}_n^{\text{in}}(\omega) = \left[\hat{S}(\omega) - 1\right] \hat{v}_n^{\text{out}}(\omega) \Rightarrow \\ &v_n^{\text{in}}(t) = -v_n^{\text{out}}(t) + \int_{-\infty}^{\infty} s(\tau) v_n^{\text{out}}(t - \tau) \, d\tau. \end{aligned} \tag{9}$$

The ADE formulation requires the complex wall softness coefficient to be re-cast into a summation of partial fractions with complex residues $\mu_k$ and poles $p_k$. This form of the wall softness can be

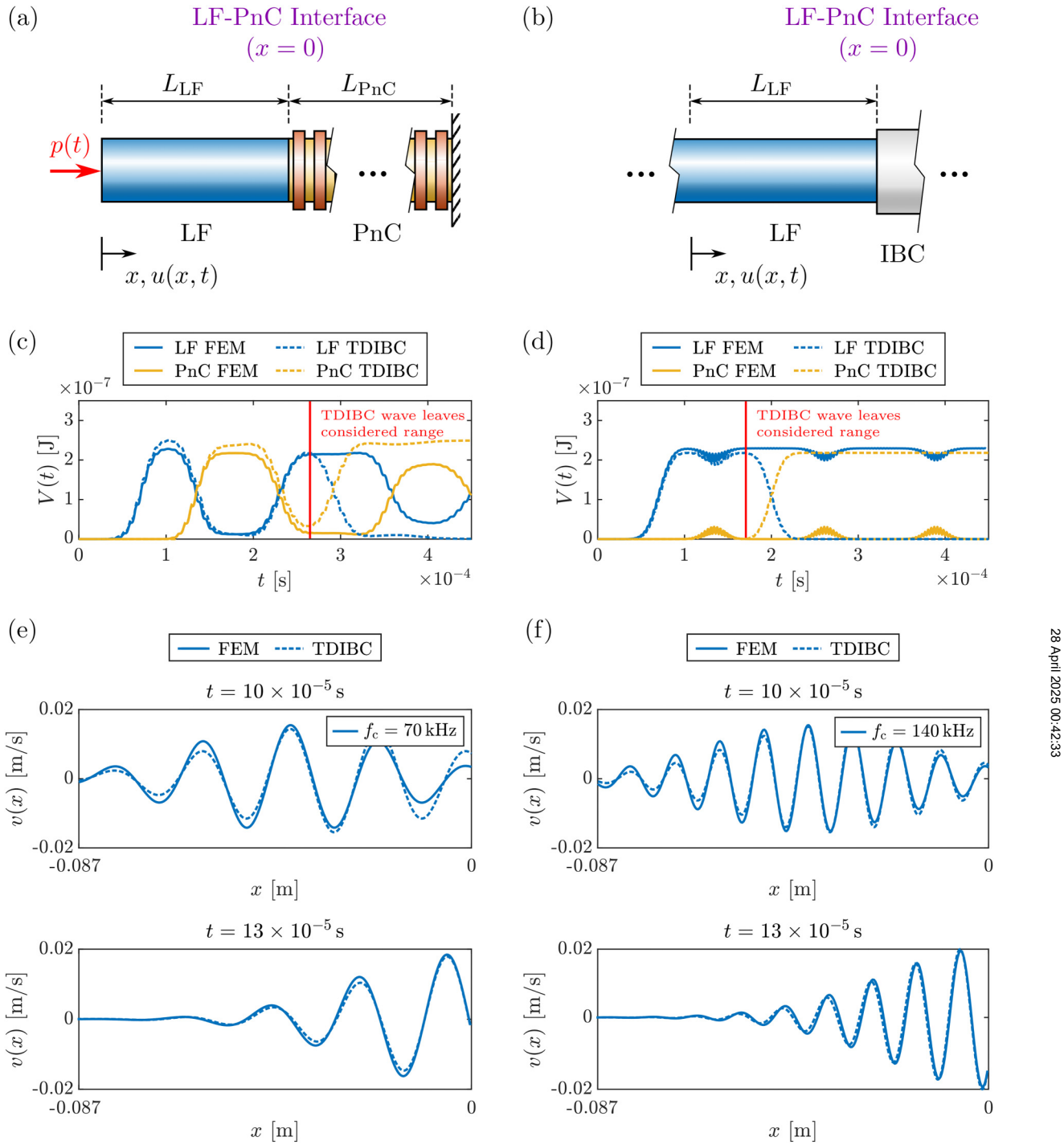


**FIG. 3.** Comparison between FEM and TDIBC. (a) Schematic diagram of an LF–PnC system where the PnC segment is fully spatially described. (b) Schematic diagram of the same system with the PnC represented by an effective impedance boundary condition (IBC). (c) and (d) Energies contained within the two segments, LF and PnC, at any given time instant throughout the simulated interval for the same two excitations used in Fig. 2, obtained via FEM (solid curves) and a time-domain impedance boundary condition (TDIBC) approach (dashed curves). Vertical solid lines in both diagrams denote the instants at which the TDIBC wave within the LF leaves the range considered by FEM. (e) and (f) Comparison between the FEM and TDIBC spatial wave profiles within the LF at 0.1 and 0.13 ms for both excitations.

inverse transformed to the time domain as

$$\hat{S}(\omega) = \sum_{k=1}^{n_0} \left( \frac{\mu_k}{i\omega - p_k} + \frac{\mu_k^*}{i\omega - p_k^*} \right) \Rightarrow s(t) = \sum_{k=1}^{n_0} \left( \mu_k e^{p_k t} + \mu_k^* e^{p_k^* t} \right) H(t), \tag{10}$$

where $H(t)$ is the Heaviside function. The complex residues and poles are obtained by performing a rational function fitting on the wall softness in the frequency space. $n_0$ in the above equation can be interpreted as the order of the functional fitting, and the partial fraction form can be interpreted as the linear superposition of $n_0$ harmonic oscillators. In this work, the vector fitting approach given by Gustavsen and Semlyen[54] is used, where a least square fit of the wall softness is performed. From Eqs. (9) and (10), it is clear that for a given incoming wave $v_n^{\text{out}}(t)$ and a known wall softness $s(t)$, the reflected wave $v_n^{\text{in}}(t)$ can be calculated, implying a one-way causality. This calculation requires the evaluation of the convolution integral in Eq. (9), which is performed using the ADE approach as detailed in Chen and Scalo.[51]

The comparison of the TDIBC approach with the FEM begins by examining the amount of energy stored in each layer, LF and PnC, as depicted in Figs. 3(c) and 3(d) for the same excitation described by Eq. (4) with $f_c = 70$ kHz (PB) and $f_c = 140$ kHz (BG), respectively. In the first, both methods lead to almost identical results for $t \leq 0.27$ ms. The results obtained from both methods understandably deviate for $t > 0.27$ ms, since the TDIBC uses a longer LF layer, and the wave leaves the range considered in the FEM simulation. In the second case, the pressure excitation falls within the PnC's BG and is therefore reflected at the LF–PnC interface. As a result, the TDIBC wave leaves the FEM range earlier and the results align for $t \leq 0.17$ ms. Figures 3(e) and 3(f) show a comparison between the spatial wave profiles within the LF obtained from both methods, corresponding to both excitations, and at two different time instants. At 0.1 ms, the wave is located in the mid-span of the LF, whereas at 0.13 ms, the wave hits the LF–PnC interface. Once again, both calculations show nearly coinciding results, effectively validating the use of an effective impedance boundary condition to describe the PnC and accurately capture the corresponding fluid–structural interaction.

## III. ENERGY EXTRACTION VIA A SUBSURFACE ACOUSTIC DIODE

The interaction between the LF and the PnC reveals that a pressure wave stays in the fluid column if its frequency spectrum falls within the PnC's BG. As shown in Fig. 2(d), the PnC rejects the wave at the LF–PnC interface causing energy to build up and remain confined to the fluid layer. While PnCs have been previously used to stabilize the energy associated with an unstable fluid wave, this was done by exciting a structural resonance (inside[28] or outside[38] the BG) to counter the fluid's motion at a single frequency. In here, we seek to take advantage of the wide BG range and utilize the BG itself as an energy absorption mechanism. To do so, we devise a mechanism which allows the pressure oscillation to first be transported out of the fluid into the adjacent structure and then prohibited from returning back into the fluid. For this, we design the system such that the pressure wave incident from the fluid side aligns with the PnC's PB and can therefore be transmitted from the LF to the PnC. Additionally, the PnC is appended with a structural layer which serves to alter the fundamental frequency content of the pressure wave such that it falls within the PnC's BG. As such, after propagating through the entire PnC length, $L_{\text{PnC}}$, the wave is transferred to the augmenting layer where it undergoes the aforementioned frequency change and is consequently forbidden from infiltrating the PnC medium on its way back to the fluid column. The combination of the PnC and its adjacent structure are henceforth referred to as an acoustic diode (AD), and the following sections present two different paradigms to achieve this concept.

### A. Active configuration: PnC augmented with TVM

The first configuration of the AD comprises a PnC which is augmented with a time-varying medium (TVM), as shown in Fig. 4(a). The latter is described by a stiffness profile that varies in time to instigate a change in the frequency of the propagating wave after passing through the PnC. This is henceforth denoted as the active AD configuration since the time-dependent stiffness profile requires an external energy source to achieve (see, for example, motorized rotations in Ref. 55 or piezoelectric circuits in Ref. 56). In addition to the complexity associated with imposing a time-varying stiffness in a material, another challenge of this configuration is the identification of the appropriate time instant to induce the stiffness change after the wave has entered the TVM. Nonetheless, we present this system as an "idealized scenario" for achieving the desired diode effect which we then try to mimic, to the extent possible, via passive means in the following section.

Similar to Fig. 2, a pressure wave $p(t)$ is injected into the fluid column at $x = -L_{\text{LF}}$, which is given by Eq. (4) and carries a central frequency of $f_c = 70$ kHz (see the supplementary material Movie 2). As the pressure wave propagates through the structure, the system's total energy is given by $V_{\text{tot}} = V_{\text{LF}} + V_{\text{PnC}} + V_{\text{TVM}}$, where the first two terms are described by Eqs. (5) and (6) and $V_{\text{TVM}}$ is given by

$$V_{\text{TVM}} = \frac{\rho_{\text{TVM}} A_{\text{TVM}}}{2} \int_{L_{\text{TVM}}} u_{,t}^2 \, \mathrm{d}x + \frac{E_{\text{TVM}} A_{\text{TVM}}}{2} \int_{L_{\text{TVM}}} u_{,x}^2 \, \mathrm{d}x. \tag{11}$$

These are used to compute the amount of energy contained in each layer, LF, PnC, and TVM, as shown in Fig. 4(c). The energy builds up in the LF reaching a maximum around $1.0 \times 10^{-4}$ s, at which time the incident wave is gradually transmitted from the LF into the PnC at $x = 0$. With the exception of minor reflections at the LF–PnC interface, the PnC freely admits the wave since its frequency spectrum falls within the PnC's PB, as confirmed by Figs. 1(b) and 1(c). The wave continues to propagate through the PnC medium and enters the TVM at approximately $1.6 \times 10^{-4}$ s, which marks the beginning of a gradual reduction in the energy stored within the PnC. Owing to its time-dependent stiffness profile, the elastic modulus of the TVM increases by a factor of four over a short time interval beginning at $2.2 \times 10^{-4}$ s, as

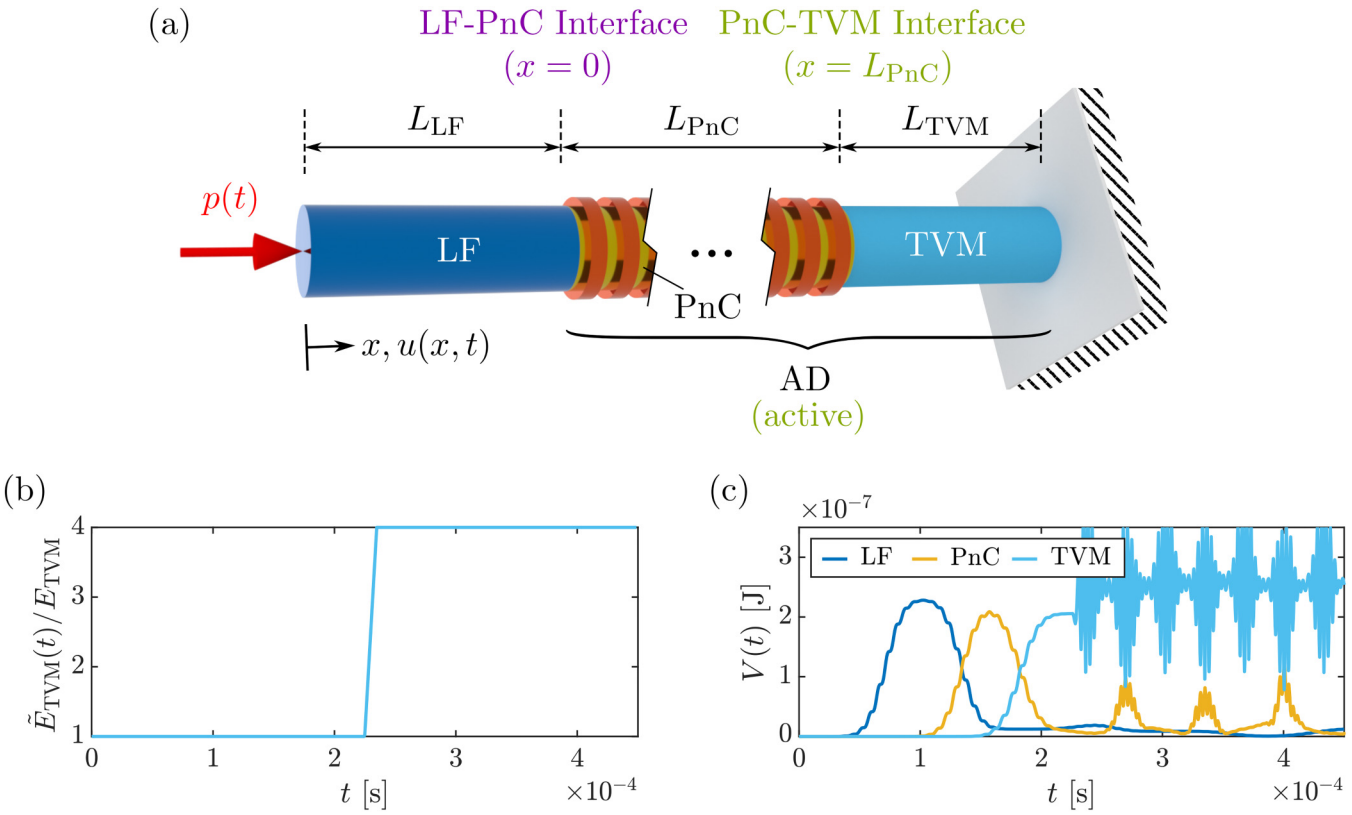


**FIG. 4.** Energy extraction from LF via an active AD configuration. (a) The LF interfaces with a 10-cell PnC which is followed by a time-varying medium (TVM) having a time-dependent stiffness profile. The PnC and TVM segments collectively from an acoustic diode (AD). The LF–PnC interface is the $x = 0$ point, the PnC-TVM interface takes place at $x = L_{\mathrm{PnC}}$, and the TVM is fixed at $x = L_{\mathrm{PnC}} + L_{\mathrm{TVM}}$. The LF is excited at $x = -L_{\mathrm{LF}}$ with a pressure pulse $p(t)$ centered around $f_c = 70$ kHz. (b) The elastic modulus of the TVM increases by a factor of four beginning at $2.2 \times 10^{-4}$ s. (c) Energies contained within the three segments, LF, PnC, and TVM (and color coded accordingly). The plot shows the energy of the incident wave first being gradually transmitted from the LF into the PnC on its forward path since its frequency lies within the PnC's PB and then enters the TVM. The TVM shifts the frequency of the reflected wave into the PnC's BG, causing it to remain confined to the TVM segment of the system, as shown by the sustained energy level within the TVM and the almost non-existent energy level within the LF after the wave has fully departed the fluid.



depicted in Fig. 4(b), and closely aligning with the instant at which the wave reflects off of the fixed TVM boundary ($x = L_{\mathrm{PnC}} + L_{\mathrm{TVM}}$) and begins traveling leftward toward the PnC. As a result of the stiffness change, the reflected wave falls squarely within the PnC's BG and is therefore rejected at the PnC-TVM interface (corresponding to $x = L_{\mathrm{PnC}}$) and is consequently trapped within the TVM segment of the acoustic diode. Figure 4(c) shows a sustained high level of the trapped energy within the TVM starting around $2.4 \times 10^{-4}$ s. It is worth noting that the energy curve associated with the fluid drops down to a negligible level once the wave fully departs the LF and never returns to its original value, confirming the diode's efficacy in almost completely extracting the energy of the incident pressure wave from the fluid column.

Figure 5 provides a closer look at the inner workings of the AD by providing snapshots of the spatial wave profile along the entire system at noteworthy time instants. Specifically, Figs. 5(a) and 5(b) show the velocity $v$ along the wave propagation direction $x$ at 0.08, 0.16, 0.32, and 0.42 ms, for LF–PnC system without and with the TVM, respectively. Vertical solid lines in all the shown results denote the LF–PnC and PnC-TVM interfaces, wherever applicable. The first shown wave profile at 0.08 ms corresponds to the input wave entirely being in the LF, while that at 0.16 ms corresponds to the wave being mostly in the PnC layer. As such, there are no significant differences between the left and rightmost plots, and the results are used as a sanity check of the simulations. The last two profiles at 0.32 and 0.42 ms clearly show the wave bouncing back into the LF in the absence of the TVM addendum, and the wave continuing to travel unimpeded from end to end. On the contrary, the rightmost plots show the wave entering and getting locked into the TVM, drastically and permanently reducing the oscillations in the LF, as desired.

### B. Passive configuration: PnC augmented with NLM

To avoid the practical challenges associated with imposing a time-varying stiffness profile within an active material, an alternative configuration of the AD is presented with the goal of extracting an undesirable pressure oscillation from a fluid in a passive

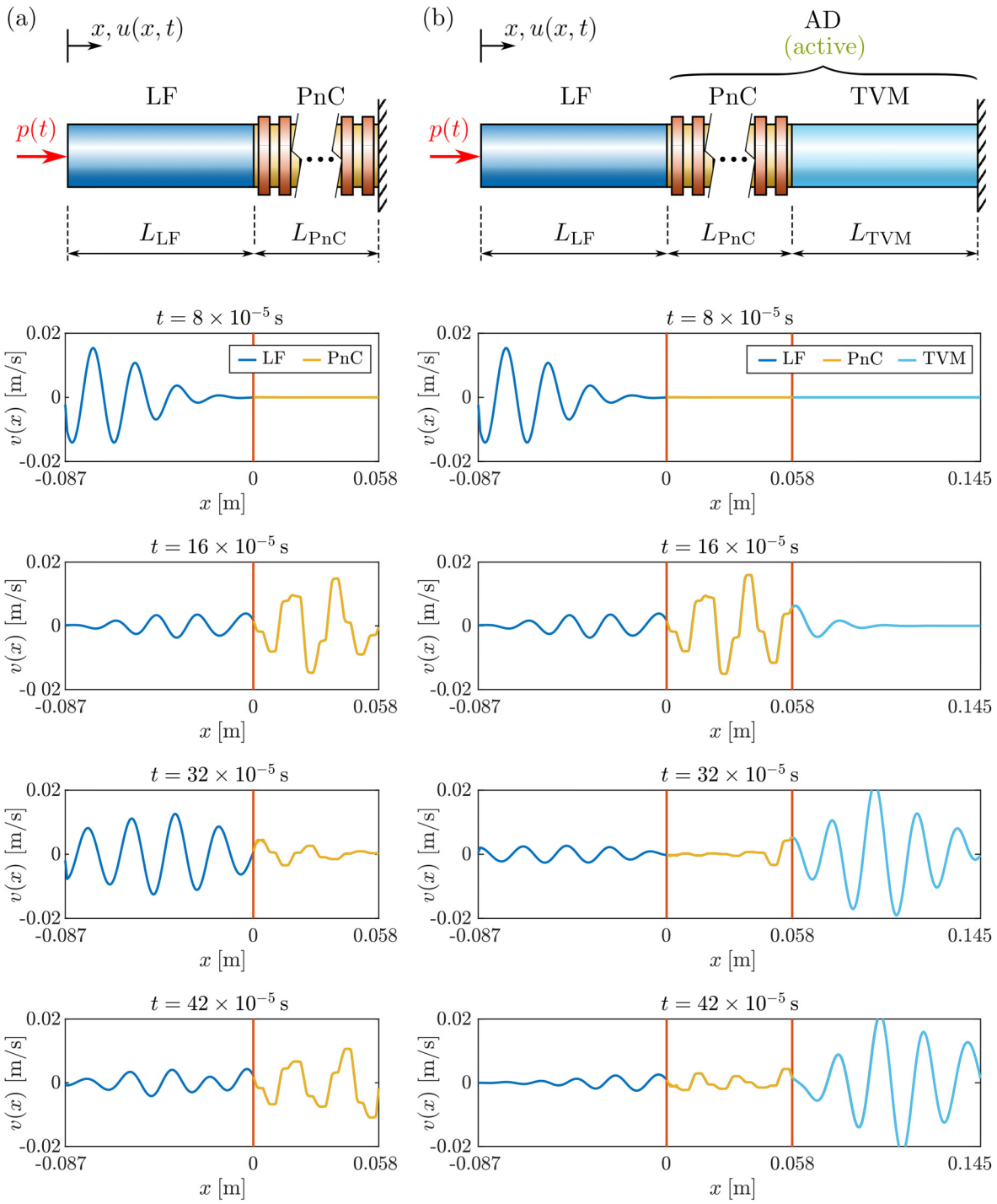


**FIG. 5.** Spatial wave profiles during energy extraction process. Schematic diagrams and spatial wave profiles for an LF–PnC system (a) without and (b) with the TVM, respectively. Plots show the velocity $v$ along the propagation direction $x$ at 0.08, 0.16, 0.32, and 0.42 ms for the same simulation described in Fig. 4. Vertical solid lines denote LF–PnC and PnC–TVM interfaces. Wave profiles at the first two time instants correspond to the early stages of pressure wave (prior to reaching the end of the PnC for the first time), and are therefore identical between the two systems. The last two time instants show the wave bouncing back into the LF in the absence of the TVM addendum in (a), in contrast to the wave being trapped in the TVM in (b), as desired.

manner. For this purpose, the AD is realized via a series connection of a PnC and a nonlinear hyperelastic material (NLM). For consistency, the PnC still consists of 10 unit cells. The total kinetic and potential energies of the LF along with the passive AD are given by

$$V_{\text{kin}} = \frac{\rho_{\text{LF}} A_{\text{LF}}}{2} \int_{L_{\text{LF}}} u_{,t}^2 \,\mathrm{d}x + \sum_{n=1}^{10} \left[ \frac{\rho_1 A_1}{2} \int_{L_1} u_{,t}^2 \,\mathrm{d}x + \frac{\rho_2 A_2}{2} \int_{L_2} u_{,t}^2 \,\mathrm{d}x \right] + \frac{\rho_{\text{NLM}} A_{\text{NLM}}}{2} \int_{L_{\text{NLM}}} u_{,t}^2 \,\mathrm{d}x \tag{12}$$

and

$$V_{\text{pot}} = \frac{E_{\text{LF}} A_{\text{LF}}}{2} \int_{L_{\text{LF}}} u_{,x}^2 \,\mathrm{d}x + \sum_{n=1}^{10} \left[ \frac{E_1 A_1}{2} \int_{L_1} u_{,x}^2 \,\mathrm{d}x + \frac{E_2 A_2}{2} \int_{L_2} u_{,x}^2 \,\mathrm{d}x \right] + \frac{E_{\text{NLM}} A_{\text{NLM}}}{2} \int_{L_{\text{NLM}}} \left( u_{,x} + \frac{1}{2} u_{,x}^2 \right)^2 \mathrm{d}x, \tag{13}$$

respectively. Additionally, the non-conservative work done by the pressure excitation can be expressed as

$$W_\delta = p(t) A_{\text{LF}} \, \delta u(x = -L_{\text{LF}}, t), \tag{14}$$

with $\delta$ being the variational operator and $\delta u(x = -L_{\text{LF}}, t)$ being the virtual displacement at the excitation point. As such, Hamilton's principle is applied as follows:

$$\delta \int_{t_0}^{t_1} \left( V_{\text{kin}} - V_{\text{pot}} \right) \mathrm{d}t + \int_{t_0}^{t_1} W_\delta \,\mathrm{d}t = 0, \tag{15}$$

for two arbitrary but constant time boundaries $t_0$ and $t_1$, which in combination with the corresponding variational calculus leads to the following equation:

$$\int_{t_0}^{t_1} \Bigg\{ A_{\text{LF}} \int_{L_{\text{LF}}} (E_{\text{LF}} u_{,x} \delta u_{,x} + \rho_{\text{LF}} u_{,tt} \delta u) \mathrm{d}x + \sum_{n=1}^{10} \Bigg[ A_1 \int_{L_1} (E_1 u_{,x} \delta u_{,x} + \rho_1 u_{,tt} \delta u) \mathrm{d}x + A_2 \int_{L_2} (E_2 u_{,x} \delta u_{,x} + \rho_2 u_{,tt} \delta u) \mathrm{d}x \Bigg] + A_{\text{NLM}} \int_{L_{\text{NLM}}} \left[ E_{\text{NLM}} \left( u_{,x} + \frac{3}{2} u_{,x}^2 \right) \delta u_{,x} + \rho_{\text{NLM}} u_{,tt} \delta u \right] \mathrm{d}x - p(t) A_{\text{LF}} \, \delta u(x = -L_{\text{LF}}, t) \Bigg\} \mathrm{d}t = 0. \tag{16}$$

It should be noted that the inertia terms in the previous equation have been already modified by using partial integration over time, and that strain terms $u_{,x}$ up to the second order only are considered. The physical and virtual displacements are approximated with the following FEM solution which is separable in space and time:

$$u \approx \mathbf{U}(x) \cdot \tilde{\mathbf{u}}(t), \quad u_{,x} \approx \mathbf{U}'(x) \cdot \tilde{\mathbf{u}}(t), \quad u_{,tt} \approx \mathbf{U}(x) \cdot \ddot{\tilde{\mathbf{u}}}(t),$$
$$\delta u \approx \mathbf{U}(x) \cdot \delta\tilde{\mathbf{u}}(t), \quad \delta u_{,x} \approx \mathbf{U}'(x) \cdot \delta\tilde{\mathbf{u}}(t), \tag{17}$$

where the row vector $\mathbf{U}(x)$ includes the shape functions and the column vector $\tilde{\mathbf{u}}(t)$ represents the nodal degrees of freedom. Together with a perturbation approach for small displacements, i.e., $\tilde{\mathbf{u}}(t) = \tilde{\mathbf{u}}_0 + \Delta\tilde{\mathbf{u}}(t)$, Eq. (16) can be rewritten as

$$\int_{t_0}^{t_1} \Bigg[ \underbrace{\left( \mathbf{M} \cdot \Delta\ddot{\tilde{\mathbf{u}}} + \mathbf{K} \cdot \Delta\tilde{\mathbf{u}} - \mathbf{f} \right)^{\text{T}}}_{=\mathbf{0}} \cdot \underbrace{\delta\tilde{\mathbf{u}}}_{\neq \mathbf{0}} \Bigg] \mathrm{d}t = 0, \tag{18}$$

where $(\dots)^{\text{T}}$ marks a matrix transpose. The point of interest for linearization is given by $\tilde{\mathbf{u}}_0$ and motion in its vicinity, i.e., $\Delta\tilde{\mathbf{u}}(t)$. Since the arbitrary virtual displacement $\delta\tilde{\mathbf{u}}(t) \neq \mathbf{0}$, the classical FEM system can be constructed, which is, respectively, described by the following mass and stiffness matrices:

$$\mathbf{M} = \rho_{\text{LF}} A_{\text{LF}} \int_{L_{\text{LF}}} \mathbf{U}^{\text{T}} \cdot \mathbf{U} \,\mathrm{d}x + \sum_{n=1}^{10} \left[ \rho_1 A_1 \int_{L_1} \mathbf{U}^{\text{T}} \cdot \mathbf{U} \,\mathrm{d}x + \rho_2 A_2 \int_{L_2} \mathbf{U}^{\text{T}} \cdot \mathbf{U} \,\mathrm{d}x \right] + \rho_{\text{NLM}} A_{\text{NLM}} \int_{L_{\text{NLM}}} \mathbf{U}^{\text{T}} \cdot \mathbf{U} \,\mathrm{d}x, \tag{19a}$$

$$\mathbf{K} = A_{\text{LF}} E_{\text{LF}} \int_{L_{\text{LF}}} \mathbf{U}'^{\text{T}} \cdot \mathbf{U}' \,\mathrm{d}x + \sum_{i=1}^{10} \left[ A_1 E_1 \int_{L_{1i}} \mathbf{U}'^{\text{T}} \cdot \mathbf{U}' \,\mathrm{d}x + A_2 E_2 \int_{L_{2i}} \mathbf{U}'^{\text{T}} \cdot \mathbf{U}' \,\mathrm{d}x \right] + A_{\text{NLM}} \underbrace{E_{\text{NLM}} (1 + 3\tilde{u}_{0,x})}_{=\tilde{E}_{\text{NLM}}} \int_{L_{\text{NLM}}} \mathbf{U}'^{\text{T}} \cdot \mathbf{U}' \,\mathrm{d}x, \tag{19b}$$

and the excitation vector

$$\mathbf{f} = p(t) A_{\text{LF}} \, \mathbf{U}(-L_{\text{LF}}). \tag{20}$$

To that end, we consider two nonlinear materials: NLM-A and NLM-B. The first comprises a nonlinear elastic modulus of pure geometrical origin, of the form[42]

$$\tilde{E}_{\text{NLM-A}} = E_{\text{NLM}} (1 + \xi \tilde{u}_{0,x}), \tag{21}$$

where $\xi \tilde{u}_{0,x}$ is a stress stiffening term and $\xi$ is an arbitrary non-dimensional value. The second utilizes an exponential strain dependency and is given by

$$\tilde{E}_{\text{NLM-B}} = E_{\text{NLM}} \left[ 1 + \eta \left( 1 - e^{-|\tilde{u}_{0,x}|/\zeta} \right) \right], \tag{22}$$

where $\eta$ and $\zeta$ are independent coefficients. For local discretization, two-noded elements with linear ansatz-functions are used. As a result, the FEM vectors of Eq. (17) for an arbitrary element $i$ can be

expressed as

$$\mathbf{U}_e = \left[\frac{1-y}{2}, \frac{y+1}{2}\right] \quad \text{and} \quad \tilde{\mathbf{u}}_e = [u_i, u_{i+1}]^T, \tag{23}$$

where the local coordinate $y \in [-1, 1]$ denotes the unit domain for integration of each element. By introducing the length of a single finite element $L_e$, the following conditions must be satisfied:

$$\left.\begin{array}{c} y(x) = a_1 + a_2 x \\ y(x = -L_e/2) \equiv -1 \\ y(x = +L_e/2) \equiv +1 \end{array}\right\} \Rightarrow \begin{array}{c} y = \frac{2}{L_e} x, \\ \partial x = \frac{L_e}{2} \partial y, \end{array} \tag{24}$$

and the global FEM matrices can be consequently assembled using the contributions of each element.

The performance of the passive AD configuration comprising the 10-cell PnC in series with each of the two NLMs is evaluated in Fig. 6 (see the supplementary material Movies 3 and 4). For the following set of results, the nonlinear parameters are chosen as follows: $\xi = 10^4$ for NLM-A, and $\eta = 3$ as well as $\zeta = \frac{\hat{p} A_{LF}}{A_{NLM} \tilde{E}_{NLM}} = 1.12 \times 10^{-5}$ for NLM-B. The goal of each of the two nonlinear media is to alter the frequency spectrum of the incident oscillation in a manner which amplifies higher harmonics of the pressure wave, thus forcing a good amount of the wave's energy into the PnC's BG range. The results obtained from the active AD are used as a benchmark and for consistency, the LF–PnC and PnC–NLM interfaces are kept at $x = 0$ and $x = L_{PnC}$, respectively. Additionally, the pressure excitation $p(t)$ still holds the same form with a central frequency of $f_c = 70$ kHz. Figure 6(b) shows the strain dependence of the elastic moduli of NLM-A and NLM-B, compared to a linear material of the same base modulus. The system's total energy is given by $V_{tot} = V_{LF} + V_{PnC} + V_{NLM-A/B}$, where the first two terms are described by Eqs. (5) and (6) and $V_{NLM-A/B}$ is given by

$$V_{NLM-A/B} = \frac{\rho_{NLM} A_{NLM}}{2} \int_{L_{NLM}} u_{,t}^2 \, dx + \frac{\tilde{E}_{NLM-A/B} A_{NLM}}{2} \int_{L_{NLM}} u_{,x}^2 \, dx. \tag{25}$$

Which are used to compute the amount of energy contained in each layer, LF, PnC, and NLM-A/B, as shown in Figs. 6(c) and 6(d). Similar to the active AD, an energy build up can be seen in the LF reaching a maximum around $1.0 \times 10^{-4}$ s, at which time the incident wave is gradually admitted into the PnC at $x = 0$. The wave enters the NLM at approximately $1.6 \times 10^{-4}$ s and the energy stored in the nonlinear medium gradually increases from this point onward. As expected, the solutions in Figs. 6(c) and 6(d) prior to this instant are nearly identical. Once the wave reaches the fixed end and bounces back, it hits the PnC-NLM interface after its frequency signature has been passively altered by the nonlinear medium. At that point, the relative amount of energy prevented from propagating through the PnC largely depends on the NLM's ability to drive up the wave's bandwidth into the PnC's BG range (computed in Fig. 1). A comparison of Figs. 6(c) and 6(d) reveals that NLM-A does a noticeably better job of trapping the pressure oscillation within the confines of the NLM layer of the AD, as evident by the large drop in the LF's and PnC's energy curves which nearly remain at the attenuated level throughout the simulation. On the contrary, while NLM-B appears to be capable of trapping some of the pressure wave, the amount of energy in the nonlinear medium drops after the wave reflects back, indicating that a decent amount of that wave was permitted by the PnC and transmitted back into the LF, as evident by the rise in the $V_{PnC}$ curves starting around $2.5 \times 10^{-4}$ s, and that of the $V_{LF}$ curves starting around $3.0 \times 10^{-4}$ s.

The obtained behavior is further explained by the results shown in Fig. 6(e) which displays the frequency spectra of the velocity at the last FEM node in the NLM layer prior to the fixed end. Compared with the frequency spectrum of the inputted pressure pulse shown in Fig. 2(c), the plots show that while both NLMs have enforced significant widening of the excitation's bandwidth, NLM-B has managed to shift the incident wave into higher frequency regimes resulting in the largely flat velocity response seen in the figure. This allows NLM-A to drive a larger portion of the pressure pulse into the PnC's BG ranges, which are shaded in the background of Fig. 6(e) for reference. Finally, the overall efficiency of the energy extraction mechanism of each of the three considered systems is quantified in Fig. 6(f) by evaluating the amount of energy trapped in the diode ($V_{tot,ex}$), i.e., PnC and augmenting layer, as a percentage of the total amount of energy initially contained in the pressure pulse exciting the LF ($V_{tot,max}$). It is found that while the active AD extracts the highest amount of undesirable energy from the fluid column at 91%, a passive AD with NLM-A used in conjunction with the PnC is able to extract 83% of the undesirable energy, compared to 50% extracted by NLM-B, for the case when $f_c = 70$ kHz which is studied here. These numbers as well as the ability of the same AD design to perform well over a broad range of perturbation frequencies depend largely on the different energy trapping mechanisms utilized by the augmenting layer in the AD, i.e., TVM vs NLM, which are detailed in the next section.

### C. Broadband operational range of subsurface acoustic diode

As explained in Sec. I, although subsurface PnCs have been deployed in different ways to impede the growth of a flow instability in recent literature, the focus of these efforts has been on targeting an unstable fluid mode assumed to be of a single frequency, to which the structural resonance of a PnC[28,39,40] or a locally resonant metamaterial[38] is tuned to trigger favorable phase conditions that lead to discernible wave cancelation. In contrast, the subsurface AD presented here is effective over a broad range of frequencies and is not constrained to single-frequency perturbations, overcoming a major limitation in current subsurface configurations. This renders it capable of targeting wave packets of frequencies clustered around a central frequency, as well as distinct single-frequency modes that fall within the AD's operational range.

Figure 7(a) qualitatively illustrates the different mechanisms by which the TVM-based (active) and the NLM-based (passive) configurations of the subsurface AD trap the energy that impinges on it from the fluid side. As seen in the left side of Fig. 7(a), the TVM layer works by directly shifting the frequency signature of the

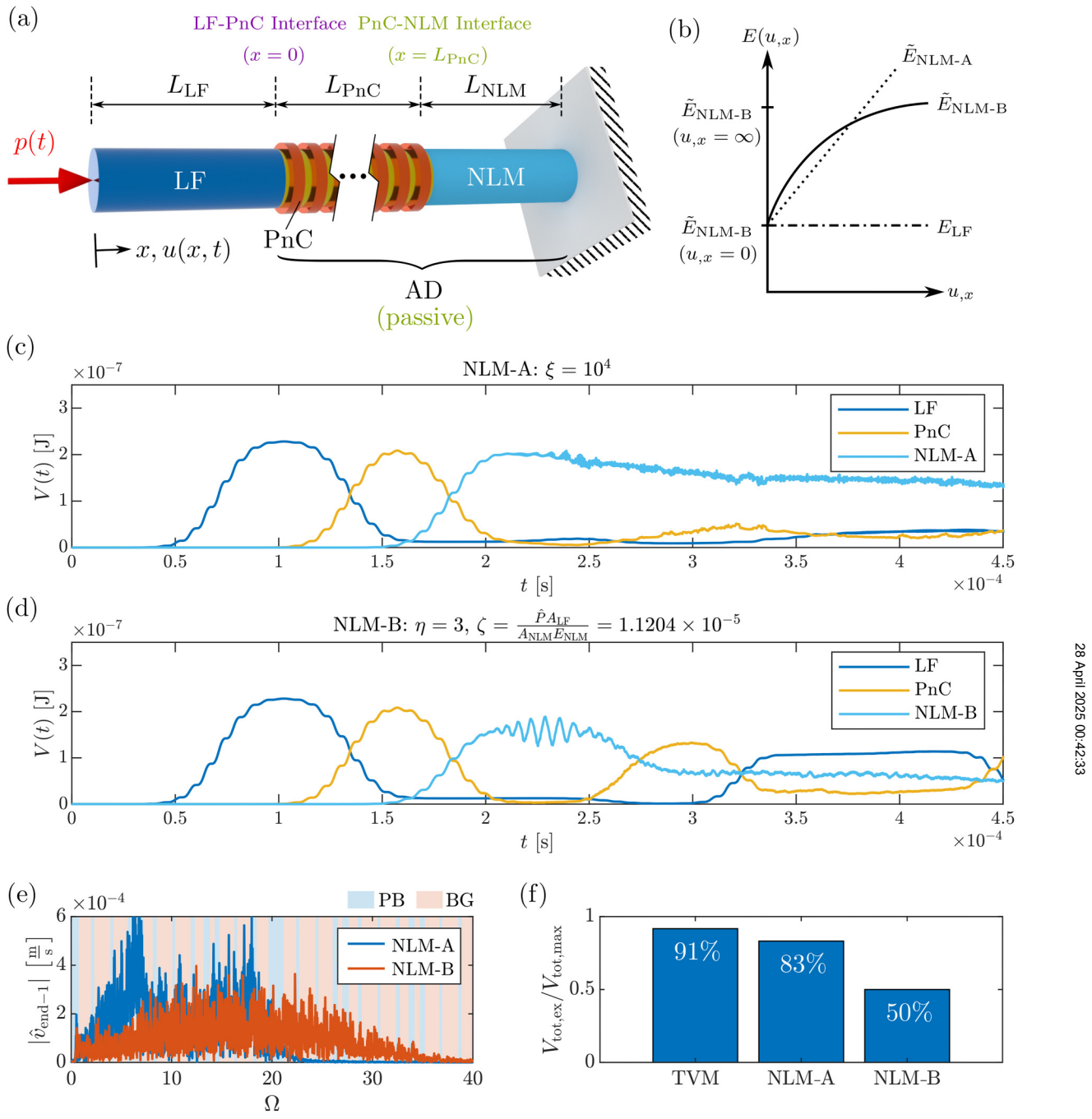


**FIG. 6.** Energy extraction from LF via a passive AD configuration. (a) The LF interfaces with a 10-cell PnC connected to a nonlinear material (NLM). The PnC and NLM segments collectively form an AD. The LF is excited at $x = -L_{\text{LF}}$ with a pressure pulse $p(t)$ centered around $f_c = 70$ kHz. (b) Strain dependence of the elastic moduli of two NLM configurations: NLM-A and NLM-B, compared to a linear material of the same base modulus. (c) and (d) Energies contained within the three segments, LF, PnC, and (c) NLM-A or (d) NLM-B. NLM-A outperforms NLM-B in trapping most of the pressure oscillation away from the LF, as evident by the large and near-permanent drop in the $V_{\text{LF}}$ curve. NLM-B allows a decent amount of the wave to be transmitted back into the PnC and consequently the LF, as evident by the rise in the $V_{\text{LF}}$ curves starting around $3.0 \times 10^{-4}$ s. (e) Frequency spectra of the velocity at the last non-fixed FEM node in the NLM layer. Both NLMs widen the bandwidth of the incident pressure wave, but NLM-A drives a larger portion into the PnC's BG ranges resulting in better energy trapping. (f) Overall energy extraction efficiency of the TVM, NLM-A, and NLM-B.

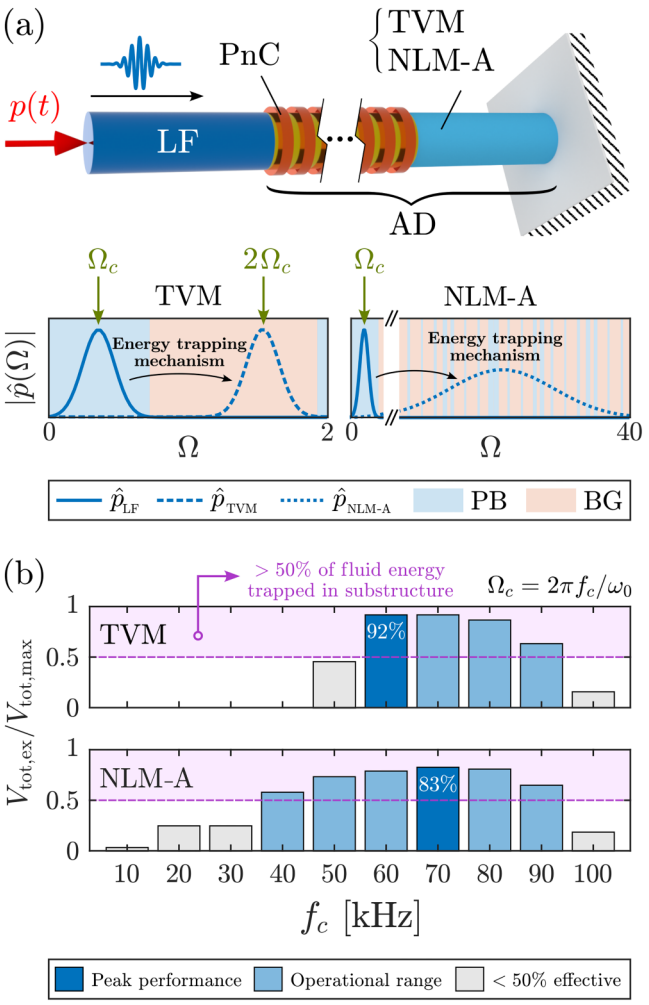


**FIG. 7.** Broadband operational range of subsurface acoustic diode. (a) Demonstration of the different energy trapping mechanisms exercised by the TVM- and NLM-based ADs. The TVM layer works by directly shifting the frequency signature of the incident perturbation from the PB to the BG of the PnC layer, while the NLM layer broadens its spectral bandwidth, both enabling the PnC to impede undesirable waves from returning to the fluid. (b) Energy trapped in the AD as a percentage of the total amount of energy initially contained in the fluid corresponding to input pressures of different central frequencies $f_c$, confirming the ability of the subsurface diode to operate effectively over a broad range of frequencies.

incident perturbation from the PB to the BG of the PnC layer, allowing the PnC to forbid the bulk of the wave from reaching the fluid layer, effectively confining it in the TVM segment. This mechanism works perfectly well in extracting undesirable pressure oscillations whose spectrum, upon transformation in the TVM, can be fully contained within the PnC's BG. This is confirmed in the top panel of Fig. 7(b) which examines the energy extraction efficiency in the same manner defined earlier (i.e., the amount of energy trapped in the diode as a percentage of the total amount of energy initially contained in the fluid), when the input pressure $p(t)$ exhibits different central frequencies. The results show that the TVM-based AD achieves stellar extraction efficiencies when the aforementioned condition is satisfied, namely, 92%, 91%, and 87%, corresponding to $f_c = 60$, 70, and 80 kHz, respectively. As can be seen in the same figure, these values drop slightly (64% for $f_c = 90$ kHz) and then significantly (46% for $f_c = 50$ kHz and 17% for $f_c = 100$ kHz) outside this window. These values are somewhat predictable given the current PnC design shown in the dispersion diagram of Fig. 1(b) and Table II, which show the BG starting at 97 kHz and ending at 253 kHz, combined with the current TVM elastic profile which shifts the frequency by a factor of two. As a result, a pressure pulse centered around 50 kHz and spanning a bandwidth of 60 kHz, for example, would result in approximately half the packet remaining inside the PnC's PB after the frequency shift, allowing it to freely propagate back into the fluid medium. Other cases considered in the figure show a near-zero extraction efficiency for $f_c < 50$ kHz, once again confirming that the TVM-based AD performs exceptionally well over a defined range of frequencies and poorly outside of it.

On the other hand, and as described by the right side of Fig. 7(a), the NLM layer of the passive AD works by flattening the frequency content of the admissible pressure, effectively widening the wave's spectrum and extending its bandwidth to much higher frequencies (notice the difference in scale on the Ω axis). The extended bandwidth spans multiple BG regions of the PnC, enabling several bands of the wave's energy to be rejected by the PnC layer on their way back to the fluid. Despite providing a lower extraction efficiency than the TVM-based AD at its peak performance (83% for $f_c = 70$ kHz), a passive AD based on NLM-A works noticeably better over a broader range of frequencies, providing more flexibility and robustness to changing conditions on the fluid side. This is confirmed in the bottom panel of Fig. 7(b), which shows extraction efficiencies exceeding 50% for undesirable pressure excitations with a central frequency that falls anywhere between 40 and 90 kHz, and a gradual decrease in effectiveness on the fringes of its operational range, showing non-zero energy extraction levels for practically every case considered.

## IV. IMPLEMENTATION OF SUBSURFACE ACOUSTIC DIODE IN FULLY DEVELOPED CHANNEL FLOW

### A. Problem setup

With the working mechanism of a subsurface AD thoroughly investigated and its effectiveness demonstrated in a simple flow-free one-dimensional setup, we examine in this section the potential of the subsurface AD to attenuate the perturbation kinetic energy contained within a two-dimensional, fully developed channel flow. Specifically, the TVM-based AD described in Sec. III A forms a 0.25-m strip which is placed underneath the surface of a 1-m long plane channel housing low-speed flow of the mock fluid (LF) described earlier at standard temperature. The top surface of the strip replaces the channel walls along the streamwise $x$-direction and extends vertically along the $y$-direction, as shown in Fig. 8. The channel has an aspect ratio of 10, with its top and bottom walls being fully rigid except at the interface with the subsurface strip (starting at $x_{AD} = 0.1$ m). The fluid domain within the channel is

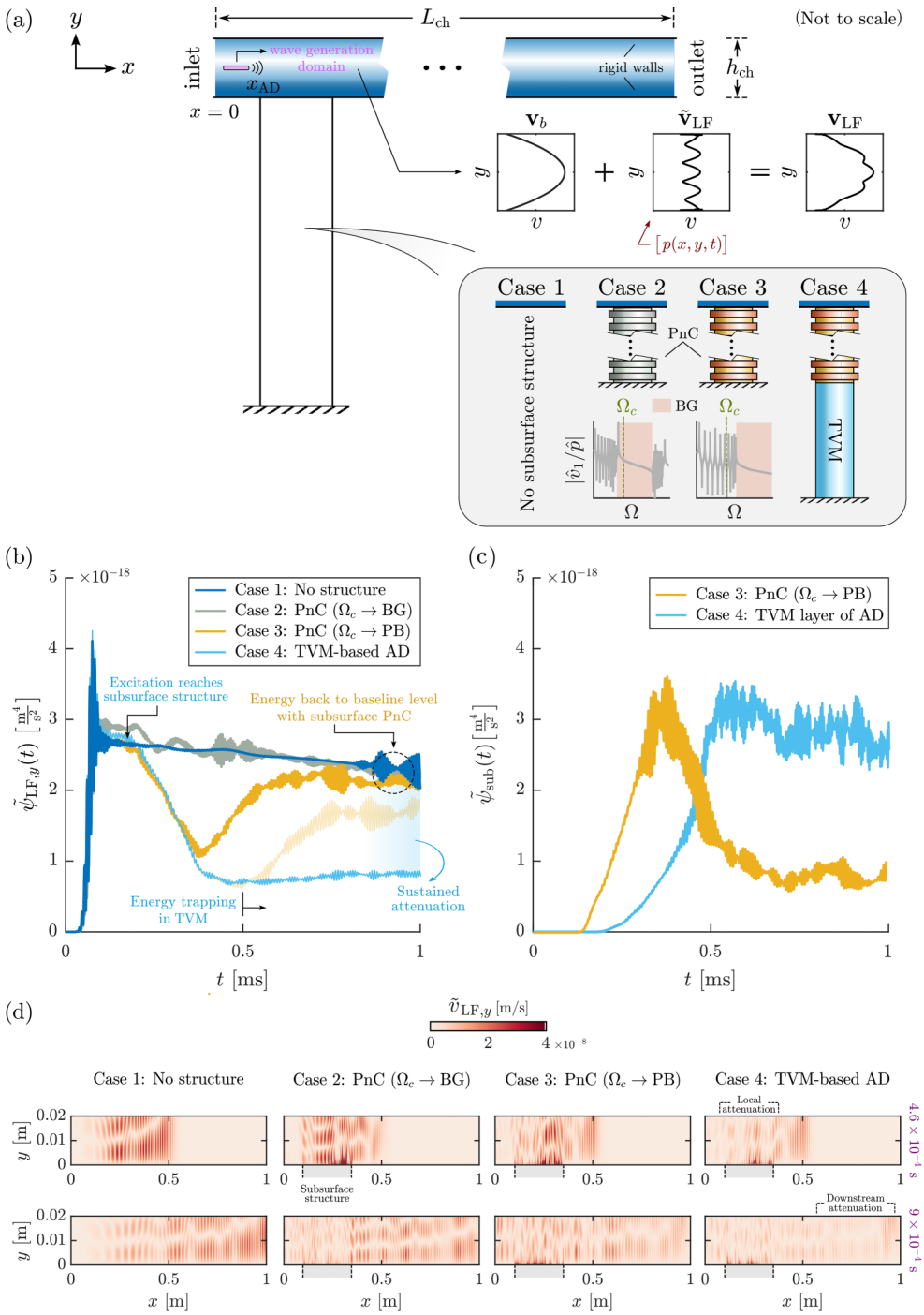


**FIG. 8.** Implementation of subsurface acoustic diode in fully developed plane channel flow. (a) Problem setup and graphical illustrations of the four cases under study. Case 1 represents a baseline system with no subsurface structure and fully rigid walls. Cases 2 and 3 include subsurface PnCs where the targeted perturbation frequency falls inside the BG or matches a resonance, respectively. Case 4 denotes the use of the TVM-based subsurface AD described in Sec. III A. (b) Fluid perturbation kinetic energy along the wall-normal $y$-direction, $\tilde{\psi}_{\mathrm{LF},y}$, for cases 1–4. The faded yellow curve shows a variation of case 3 where the PnC is made as long as the entire substructure used in case 4. (c) Kinetic energy in the subsurface structures, $\tilde{\psi}_{\mathrm{sub}}$. (d) Contours of $y$-velocity in the channel, $\tilde{v}_{\mathrm{LF},y}$, at $4.6 \times 10^{-4}$ and $9 \times 10^{-4}$ s for the four aforementioned cases.

subject to a 20 m/s inlet velocity at the left boundary ($x = 0$). The setup yields the classical Poiseuille flow, which serves as the background flow field $\mathbf{v}_b$ generated using the Fluid laminar flow interface in the CFD module of COMSOL MULTIPHYSICS. The background flow field is perturbed using the same pressure pulse $p(t)$ from Sec. II B with $f_c = 70$ kHz along a small $4 \times 0.5$ mm region at the inlet and half channel height, as denoted by the wave generation domain in Fig. 8(a). The forcing is smoothed inside this domain with oscillating functions in both directions, to yield the excitation function,

$$p_s(x, y, t) = \left[\sin\left(\pi\left[\frac{x - x_s}{\ell_s}\right]\right)\sin\left(\pi\left[\frac{y - y_s}{h_s}\right]\right)\right]p(t), \tag{26}$$

adopting a similar scheme as that outlined in Ref. 57, where $x_s$ and $y_s$ denote the starting coordinates of the wave generation domain, and $\ell_s$ and $h_s$ denote the domain's height and length, respectively. The background flow $\mathbf{v}_b$ along with the superimposed perturbation $\tilde{\boldsymbol{\nu}}_{\mathrm{LF}}$ culminate in the full flow field $\mathbf{v}_{\mathrm{LF}}$, as shown in Fig. 8(a). The Navier–Stokes equations are linearized around the background flow and then solved for the perturbed velocity and pressure fields. In the remainder of this section, the fluid's perturbation velocity components at a given location along the $x$- and $y$-directions will be denoted as $\tilde{\nu}_{\mathrm{LF},x}$ and $\tilde{\nu}_{\mathrm{LF},y}$, respectively. Two-way time-domain coupled fluid structure interaction (FSI) simulations are carried out using the Acoustics module, following which, the velocity fields in the fluid and structural domains are obtained at each time step over the duration of the simulation, and the perturbation kinetic energy in the entire fluid domain is evaluated from the surface integral of the squared velocities,

$$\tilde{\psi}_{\mathrm{LF}} = \frac{1}{2}\int_{L_{\mathrm{ch}}}\int_{h_{\mathrm{ch}}}\left(\tilde{\nu}^2_{\mathrm{LF},x} + \tilde{\nu}^2_{\mathrm{LF},y}\right)\mathrm{d}y\,\mathrm{d}x, \tag{27}$$

where $L_{\mathrm{ch}}$ and $h_{\mathrm{ch}}$ denote integrals over the length and height of the channel, respectively. The perturbed kinetic energies associated with each velocity component, i.e., $\tilde{\psi}_{\mathrm{LF},x}$ and $\tilde{\psi}_{\mathrm{LF},y}$, can be extracted from Eq. (27) by separating the integral for each component. The latter, in particular, is instrumental in understanding the fluid–subsurface interaction dynamics since the elastic structure beneath the interaction surface deforms longitudinally along the $y$-direction.[58] Additionally, upon being impinged on by the fluid, the perturbed kinetic energy contained within the subsurface structure, $\tilde{\psi}_{\mathrm{sub}}$, is similarly computed and used for further analysis.

The coupling between the fluid and structural domains is performed in COMSOL by ensuring continuity of the displacement and stress fields at the interface. The domains are discretized via 193 000 quadratic Lagrange elements. A time step that captures 14 periods of the wave's central frequency is used in a segregated solver where the pressure and velocity fields in the fluid and structural domains are solved for separately at each time step, while ensuring the coupling conditions are satisfied. The second order generalized alpha implicit method with minimal damping was used as the time-marching numerical integrating scheme. Four distinct scenarios, referred to here as "cases" 1–4, are investigated to showcase the interaction mechanisms that underlie different variations of elastic subsurface structures. Case 1 denotes the baseline (reference) scenario where no subsurface structure is utilized and all-rigid walls are used throughout the channel. Cases 2 and 3 entail the use of a subsurface PnC designed such that the targeted fluid perturbation frequency falls inside the PnC's BG or matches a PB resonance, respectively. Case 4 denotes the use of subsurface AD described in Sec. III A which consists of a PnC augmented with a TVM layer. A graphical depiction of the four cases can be seen in the inset of Fig. 8.

### B. Results

Figure 8(b) shows the variation of $\tilde{\psi}_{\mathrm{LF},y}$ over $1 \times 10^{-3}$ s for the four aforementioned cases. Examining the curve associated with case 1 enables us to understand the baseline behavior associated with the perturbation-infused channel flow in the absence of a subsurface structure. The generated wave results in an energy build up which reaches a peak around $0.75 \times 10^{-4}$ s, and the wave propagates freely through the channel reaching the right end around $8.1 \times 10^{-4}$ s, with some increased oscillations happening shortly thereafter due to back scattering. Case 2 reveals a pattern which is largely similar to the baseline case, primarily due to the inability of the subsurface structure to absorb fluid energy as a result of the bulk wave falling inside the PnC's BG. Consequently, the structure continuously rejects the impinging waves limiting the oscillations to its first few unit cells (typical of a finite PnC response inside a BG[45]), and resulting in minimal periodic oscillations around the baseline $\tilde{\psi}_{\mathrm{LF},y}$ level without much of a net effect. Case 3 is closest in nature to the approach most prevalent in literature whereby the excitation aligns with a resonant PnC mode, triggering wave propagation through the PnC away from the flow as soon as the excitation reaches the subsurface strip around $1.5 \times 10^{-4}$ s. This energy transmission from the fluid to the PnC in itself results to a noticeable drop in $\tilde{\psi}_{\mathrm{LF},y}$ until $3.9 \times 10^{-4}$ s. This drop is, however, short lived, as the waves thereafter reflect at the fixed end of the PnC and return to the fluid, thus reversing the slope of the curve and gradually raising the energy level. This is evident by the near-complete return of $\tilde{\psi}_{\mathrm{LF},y}$ to its baseline level around $6.6 \times 10^{-4}$ s. However, a small but noticeable attenuation persists following this time instant which can be attributed to the canceling effect induced by the out-of-phase waves reentering the flow after resonating within the PnC, as detailed in Refs. 28, 39 , and 59, among others.

The ability of the subsurface AD to extract the perturbation energy from the flow, in a manner superior to the comparison cases, is exemplified by case 4 in Fig. 8(b). Similar to case 3, the input wave reaches the strip at $x_{\mathrm{AD}}$ around $1.5 \times 10^{-4}$ s into the simulation. As detailed in Sec. III A, the excitation's spectrum falls within the PnC's PB allowing it to admit the incident wave through the PnC and into the TVM layer, resulting in an uninterrupted reduction of flow energy all the way until $4.6 \times 10^{-4}$ s. This initial phase of attenuation, corresponding to energy transmission from the fluid into the subsurface AD, resembles the behavior of case 3, albeit significantly stronger in part due to the extended structure length as a result of adding the auxiliary TVM layer (For reference, the faded yellow curves show the behavior of case 3 if the PnC layer was as long as the entire substructure used in case 4). By this time instant, the bulk of the perturbation energy has reached the

TVM layer, and the TVM has completely undergone the stiffness change described in Fig. 4(b). From this point onward, and as a result of these synchronous effects, the AD succeeds in containing the perturbation energy within the TVM, effectively sustaining the perturbation energy level in the fluid at its minimum value. By the end of the simulation, the terminal $\tilde{\psi}_{\mathrm{LF},y}$ value in case 4 is remarkably 34.8% and 18.8% of the terminal and peak values encountered in the baseline case 1, respectively. This enhanced attenuation within the AD is further corroborated in Fig. 8(c) which depicts the evolution of kinetic energy inside different solids beneath the fluid surface, namely, the PnC of case 3 and the TVM layer of the subsurface AD used in case 4. While both curves temporarily rise during the initial attenuation phase described earlier, the AD's energy extraction mechanism enables it to trap approximately 73.1% of the energy that was initially admitted into the TVM within its confines, achieving steady and sustained attenuation of the flow perturbation energy that is not otherwise possible. Finally, it is worth noting that the same AD was able to achieve an energy extraction efficiency of 91% in the one-dimensional setup (see Figs. 5 and 7), signaling better performance in a simplified setup, which is expected due to the idealized conditions in the absence of flow dynamics, yet still indicative of the AD's potential to produce a meaningful impact in the context of flow stabilization.

Finally, Fig. 8(d) shows the contours of the perturbed fluid velocity along the wall-normal $y$-direction, $\tilde{v}_{\mathrm{LF},y}$, at two time instants: $4.6 \times 10^{-4}$ and $9 \times 10^{-4}$ s. The first corresponds to the excited wave reaching approximately half the channel's length, as can be seen in the case 1 (baseline) plot, while the second marks an instant near the end of the simulation where it is evident that the excited wave has reached the right end of the channel. The location of the subsurface structure is marked on the plots corresponding to cases 2–4. Compared to the baseline case, and that equipped with the two different PnCs configurations, it is seen that the setup with the subsurface AD strip exhibits both superior localized attenuation at the location of the strip (see rightmost, upper panel) and significant downstream attenuation that can be observed in the perturbation velocity contours at post-strip regions along the streamwise flow direction in the rightmost lower panel of Fig. 8(d), showing the ability of the subsurface AD to induce sustainable energy attenuation across time (i.e., the duration of the simulation) and space (the length of the channel).

## V. CONCLUSIONS

In this work, we have explored a novel approach for efficient energy extraction from a linear fluid (LF) column via a subsurface acoustic diode (AD) which distills out an undesirable pressure wave via frequency-dependent interactions. The AD consists of a bi-layered phononic crystal (PnC) which directly interfaces with the fluid column and an auxiliary medium that serves as a terminal energy sink. The PnC exhibits clear passband (PB) and bandgap (BG) ranges of free and forbidden wave transmission, respectively. The PnC is engineered such that the incident excitation falls within its PB range enabling the pressure oscillation to first be transmitted from the fluid into the structure. The auxiliary medium is synthesized from an active time-varying medium (TVM) or as a passive nonlinear medium (NLM). Both paradigms target the same goal, which is to permanently retain an incident wave once it enters the auxiliary medium by altering its spectral content to fall within the PnC's BG. In the active realization of the AD, the TVM is described by a time-dependent stiffness which induces a desired frequency change of the propagating wave after passing through the PnC, following a step-up of the elastic modulus. The passive NLM-based AD achieves the same behavior by utilizing two different nonlinear material models, thereby foregoing the need for temporal stiffness changes via external stimulation.

Initially, the dispersion characteristics of the PnC are studied. Focus is placed on the first PB and the first BG for a bi-layered rod composed of ABS and aluminum. A reference case involving a simple interaction between an LF and a PnC in the absence of an auxiliary medium is first investigated. This reference case shows the inability of a PnC to solely achieve the desired energy extraction and serves as a benchmark for the rest of the study. Following which, a comprehensive fluid-structural analysis of the scenarios associated with all AD configurations is carried out via transient finite element simulations. The wave propagation pattern, as well as the spatial and temporal energy distribution in the different fluid and structural layers, are described for all AD versions. The fluid–structure system dynamics are described using an energy-based method, applying Hamilton's principle to evaluate the constitutive motion equations, and a time-domain impedance boundary condition approach is used to verify the derived framework. The effectiveness of the proposed approach is evaluated by quantifying the percentage of energy successfully extracted from the fluid column. The TVM-based AD exhibits the highest efficiency, extracting nearly 91% of the energy of the pressure pulse in the fluid, although its effectiveness depends on the chosen time-dependent stiffness profile and choosing the appropriate moment for its onset. Practical implementations therefore necessitate continuous monitoring of the TVM's motion and, for continuous excitation, ongoing stiffness adjustments. These limitations are mitigated by employing one of the two passive NLM-based AD versions, which achieve energy extraction efficiencies of 83% and 50% for the same conditions. Further, we have successfully demonstrated the broadband operational range of the AD by computing its energy extraction effectiveness for a series of perturbations that span a wide range of different frequencies from 10 to 100 kHz, illustrating the ability of such configuration to overcome a major limitation of current systems which only target a single frequency, hindering their ability to stabilize flow instabilities with broader spectral properties or requiring a complete redesign of the subsurface following a change in the perturbation frequency. Finally, we concluded by embedding the AD beneath the surface of a two-dimensional, fully developed plane channel flow, showing its ability to attenuate the perturbation energy contained within the fluid domain. Compared to the fully rigid channel, and that equipped with two different forms of subsurface PnCs, the setup with the subsurface AD strip exhibits: (1) Sustained rather than temporary attenuation that endures through the problem, and (2) downstream attenuation that is visibly identifiable from the perturbation velocity contours at post-strip regions along the streamwise flow direction. The combined analytical–numerical foundation presented here provides a pathway for efficient extraction of a perturbation from an oscillating fluid using a fine-needle approach, which leaves minimal

residual energy and eliminates the prospect of perturbation recovery in the fluid medium. While the disturbances interacting with the mean flow used in this study were not unstable in nature, this framework paves the way for future explorations of this concept in complex wall-bounded flows with growing perturbations and streamwise instabilities that progressively grow in amplitude.

## SUPPLEMENTARY MATERIAL

See the supplementary material for four video files. Movie 1 shows the wave propagation profile and the evolution of energy levels with time and space in the one-dimensional LF–PnC, with two excitations corresponding to $f_c = 70$ and 140 kHz, respectively. Movie 2 shows the same data for the LF-AD case with the TVM-based auxiliary layer. Movies 3 and 4 show the same data when NLM-A and NLM-B are used for the auxiliary layer, respectively.

## ACKNOWLEDGMENTS

The authors acknowledge support by the U.S. Air Force Office of Scientific Research (AFOSR) under Award No. FA9550-23-1-0564.

## AUTHOR DECLARATIONS

### Conflict of Interest

The authors have no conflicts to disclose.

### Author Contributions

R.S. and H.Y. contributed equally to this work.

### Author Contributions

**R. Schmidt:** Formal analysis (lead); Investigation (lead); Software (lead); Visualization (equal); Writing – original draft (lead). **H. Yousef:** Formal analysis (supporting); Investigation (supporting). **I. Roy:** Formal analysis (supporting); Investigation (supporting); Methodology (equal); Writing – original draft (supporting). **C. Scalo:** Formal analysis (equal); Funding acquisition (equal); Project administration (equal); Resources (equal). **M. Nouh:** Conceptualization (lead); Funding acquisition (lead); Project administration (lead); Resources (lead); Visualization (lead); Writing – review & editing (lead).

## DATA AVAILABILITY

The data that support the findings of this study are available within the article.

## REFERENCES

[1]M.-C. Hsu and Y. Bazilevs, "Fluid–structure interaction modeling of wind turbines: Simulating the full machine," Comput. Mech. **50**, 821 (2012).
[2]R. Kamakoti and W. Shyy, "Fluid–structure interaction for aeroelastic applications," Prog. Aerosp. Sci. **40**, 535 (2004).
[3]G. Bertaglia, V. Caleffi, and A. Valiani, "Modeling blood flow in viscoelastic vessels: The 1D augmented fluid–structure interaction system," Comput. Methods Appl. Mech. Eng. **360**, 112772 (2020).
[4]H. W. Emmons, "The laminar-turbulent transition in a boundary layer—Part I," J. Aeronaut. Sci. **18**, 490 (1951).
[5]E. Laurien and L. Kleiser, "Numerical simulation of boundary-layer transition and transition control," J. Fluid Mech. **199**, 403 (1989).
[6]C. M. Langel, R. Chow, C. C. P. Van Dam, M. A. Rumsey, D. C. Maniaci, R. S. Ehrmann, and E. B. White, "A computational approach to simulating the effects of realistic surface roughness on boundary layer transition," in *52nd Aerospace Sciences Meeting* (AIAA, 2014), p. 0234.
[7]M. Costantini, "Experimental analysis of geometric, pressure gradient and surface temperature effects on boundary-layer transition in compressible high Reynolds number flows," Ph.D. thesis (Rheinisch-Westfälische Technische Hochschule Aachen, 2016).
[8]R. García-Mayoral and J. Jiménez, "Drag reduction by riblets," Philos. Trans. R. Soc. Lond. A **369**, 1412 (2011).
[9]M. Walsh and A. Lindemann, "Optimization and application of riblets for turbulent drag reduction," in *22nd Aerospace Sciences Meeting* (AIAA, 1984), p. 347.
[10]P. Viswanath, "Aircraft viscous drag reduction using riblets," Prog. Aerosp. Sci. **38**, 571 (2002).
[11]K. B. Golovin, J. W. Gose, M. Perlin, S. L. Ceccio, and A. Tuteja, "Bioinspired surfaces for turbulent drag reduction," Philos. Trans. R. Soc. Lond. A **374**, 20160189 (2016).
[12]A. Rastegari and R. Akhavan, "On the mechanism of turbulent drag reduction with super-hydrophobic surfaces," J. Fluid Mech. **773**, R4 (2015).
[13]B. Wang, J. Wang, Z. Dou, and D. Chen, "Investigation of retention of gases in transverse hydrophobic microgrooved surfaces for drag reduction," Ocean Eng. **79**, 58 (2014).
[14]M. Gad-el Hak, "Compliant coatings for drag reduction," Prog. Aerosp. Sci. **38**, 77 (2002).
[15]K.-S. Choi, X. Yang, B. Clayton, E. Glover, M. Atlar, B. Semenov, and V. Kulik, "Turbulent drag reduction using compliant surfaces," Proc. R. Soc. Lond., Ser. A **453**, 2229 (1997).
[16]T. Michelis, C. De Koning, and M. Kotsonis, "On the interaction of Tollmien–Schlichting waves with a wall-embedded Helmholtz resonator," Phys. Fluids **35**, 034104 (2023).
[17]G. Dacome, R. Siebols, and W. J. Baars, "Inner-scaled Helmholtz resonators with grazing turbulent boundary layer flow," arXiv:2308.07776 (2023).
[18]A. Seifert, S. Eliahu, D. Greenblatt, and I. Wygnanski, "Use of piezoelectric actuators for airfoil separation control," AIAA J. **36**, 1535 (1998).
[19]J. Choi, W.-P. Jeon, and H. Choi, "Control of flow around an airfoil using piezoceramic actuators," AIAA J. **40**, 1008 (2002).
[20]D. Haller, A. Paetzold, N. Goldin, S. Neiss, F. Goldschmidtboeing, W. Nitsche, R. King, and P. Woias, "Cymbal type piezo-polymer-composite actuators for active cancellation of flow instabilities on airfoils," in *2011 16th International Solid-State Sensors, Actuators and Microsystems Conference* (IEEE, 2011), pp. 494–497.
[21]M. Baumann and W. Nitsche, "Experiments on active control of Tollmien–Schlichting waves on a wing," in *New Results in Numerical and Experimental Fluid Mechanics: Contributions to the 10th AG STAB/DGLR Symposium Braunschweig, Germany 1996* (Springer, 1997), pp. 56–63.
[22]M. Engert, A. Pätzold, R. Becker, and W. Nitsche, "Active cancellation of Tollmien–Schlichting instabilities in compressible flows using closed-loop control," in *IUTAM Symposium on Flow Control and MEMS: Proceedings of the IUTAM Symposium held at the Royal Geographical Society, 19–22 September 2006, hosted by Imperial College, London, England* (Springer, 2008), pp. 319–331.
[23]D. Sturzebecher and W. Nitsche, "Active cancellation of Tollmien–Schlichting instabilities on a wing using multi-channel sensor actuator systems," Int. J. Heat Fluid Flow **24**, 572 (2003).
[24]A. Aladwani, A. Almandeel, and M. Nouh, "Fluid-structural coupling in metamaterial plates for vibration and noise mitigation in acoustic cavities," Int. J. Mech. Sci. **152**, 151 (2019).
[25]J. Park, J. R. Youn, and Y. S. Song, "Fluid-flow rotator based on hydrodynamic metamaterial," Phys. Rev. Appl. **12**, 061002 (2019).

[26]J. Park, J. R. Youn, and Y. S. Song, "Hydrodynamic metamaterial cloak for drag-free flow," Phys. Rev. Lett. **123**, 074502 (2019).
[27]T. Pagliaroli, F. Patanè, A. Pagliaro, P. Lv, and A. Tatí, "Metamaterials for hypersonic flow control: Experimental tests on novel ultrasonically absorptive coatings," in *2018 5th IEEE International Workshop on Metrology for AeroSpace (MetroAeroSpace)* (IEEE, 2018), pp. 284–289.
[28]M. I. Hussein, S. Biringen, O. R. Bilal, and A. Kucala, "Flow stabilization by subsurface phonons," Proc. R. Soc. Lond. A **471**, 20140928 (2015).
[29]H. Al Ba'Ba'A, C. L. Willey, V. W. Chen, A. T. Juhl, and M. Nouh, "Theory of truncation resonances in continuum rod-based phononic crystals with generally asymmetric unit cells," Adv. Theory Simul. **6**, 2200700 (2023).
[30]H. B. A. Babaa, H. Yousef, M. Nouh *et al.*, "A blueprint for truncation resonance placement in elastic diatomic lattices with unit cell asymmetry," JASA Express Lett. **4**, 077501 (2024).
[31]R. W. Milling, "Tollmien–Schlichting wave cancellation," Phys. Fluids **24**, 979 (1981).
[32]M. Baumann and W. Nitsche, "Passive control of laminar boundary-layer instabilities with phononic sub-surfaces," in *1st European Fluid Dynamics Conference* (European Mechanics Society, 2024).
[33]D. Flores Caban, "Numerical study of passive flow stabilization using resonating metamaterials," Master's thesis (Universitat Politècnica de Catalunya, 2024).
[34]C. J. Barnes, C. L. Willey, K. Rosenberg, A. Medina, and A. T. Juhl, "Initial computational investigation toward passive transition delay using a phononic subsurface," in *AIAA Scitech 2021 Forum* (AIAA, 2021), p. 1454.
[35]S. Balasubramanian, S. Park, K. Matlack, and A. Goza, "Harnessing phononic materials for aerodynamic flow control," in *AIAA Aviation 2022 Forum* (AIAA, 2022), p. 3240.
[36]A. Machado Burgos, S. Park, N. O'Brien, K. H. Matlack, and A. Goza, "Fluid-structure interaction between an unsteady vortex-driven aerodynamic flow and a diatomic phononic subsurface," in *AIAA SCITECH 2024 Forum* (AIAA, 2024), p. 1353.
[37]J. D. Navarro, J. C. C. Velasquez, E. J. LaLonde, E. N. Hoffman, C. S. Combs, and D. Restrepo, "Flow control of hypersonic shock-wave/boundary-layer interactions using phononic metamaterials," in *AIAA SCITECH 2024 Forum* (AIAA, 2024), p. 0031.
[38]A. Kianfar and M. I. Hussein, "Local flow control by phononic subsurfaces over extended spatial domains," J. Appl. Phys. **134**, 094701 (2023).
[39]T. Michelis, A. Putranto, and M. Kotsonis, "Attenuation of Tollmien–Schlichting waves using resonating surface-embedded phononic crystals," Phys. Fluids **35**, 044101 (2023).
[40]A. Kianfar and M. I. Hussein, "Phononic-subsurface flow stabilization by subwavelength locally resonant metamaterials," New J. Phys. **25**, 053021 (2023).
[41]C. L. Willey, C. J. Barnes, V. W. Chen, K. Rosenberg, A. Medina, and A. T. Juhl, "Multi-input multi-output phononic subsurfaces for passive boundary layer transition delay," J. Fluids Struct. **121**, 103936 (2023).
[42]B. Liang, B. Yuan, and J.-C. Cheng, "Acoustic diode: Rectification of acoustic energy flux in one-dimensional systems," Phys. Rev. Lett. **103**, 104301 (2009).
[43]A. H. Aly, A. Mehaney, and E. Abdel-Rahman, "Study of physical parameters on the properties of phononic band gaps," Int. J. Mod. Phys. B **27**, 1350047 (2013).
[44]A. Mehaney, "Phononic crystal as a neutron detector," Ultrasonics **93**, 37 (2019).
[45]H. Al Ba'Ba'A and M. Nouh, "An investigation of vibrational power flow in one-dimensional dissipative phononic structures," J. Vib. Acoust. **139**, 021003 (2017).
[46]H. B. Al Ba'ba'a and M. Nouh, "The role of frequency and impedance contrasts in bandgap closing and formation patterns of axially-vibrating phononic crystals," J. Appl. Mech. **91**, 031006 (2024).
[47]S. Nagarajan, S. K. Lele, and J. H. Ferziger, "A robust high-order compact method for large eddy simulation," J. Comput. Phys. **191**, 392 (2003).
[48]Y. Chen and C. Scalo, "Trapped waves in supersonic and hypersonic turbulent channel flow over porous walls," J. Fluid Mech. **920**, A24 (2021).
[49]V. C. B. Sousa and C. Scalo, "A unified quasi-spectral viscosity (QSV) approach to shock capturing and large-eddy simulation," J. Comput. Phys. **459**, 111139 (2022).
[50]Q. Douasbin, C. Scalo, L. Selle, and T. Poinsot, "Delayed-time domain impedance boundary conditions (D-TDIBC)," J. Comput. Phys. **371**, 50 (2018).
[51]Y. Chen and C. Scalo, "Effects of porous walls on near-wall supersonic turbulence," Phys. Rev. Fluids **6**, 084607 (2021).
[52]D. Dragna, P. Pineau, and P. Blanc-Benon, "A generalized recursive convolution method for time-domain propagation in porous media," J. Acoust. Soc. Am. **138**, 1030 (2015).
[53]K.-Y. Fung and H. Ju, "Time-domain impedance boundary conditions for computational acoustics and aeroacoustics," Int. J. Comput. Fluid Dyn. **18**, 503 (2004).
[54]B. Gustavsen and A. Semlyen, "Rational approximation of frequency domain responses by vector fitting," IEEE Trans. Power Delivery **14**, 1052 (1999).
[55]M. Attarzadeh, J. Callanan, and M. Nouh, "Experimental observation of nonreciprocal waves in a resonant metamaterial beam," Phys. Rev. Appl. **13**, 021001 (2020).
[56]J. Marconi, E. Riva, M. Di Ronco, G. Cazzulani, F. Braghin, and M. Ruzzene, "Experimental observation of nonreciprocal band gaps in a space-time-modulated beam using a shunted piezoelectric array," Phys. Rev. Appl. **13**, 031001 (2020).
[57]M. Kotsonis, R. Giepman, S. Hulshoff, and L. Veldhuis, "Numerical study of the control of Tollmien–Schlichting waves using plasma actuators," AIAA J. **51**, 2353 (2013).
[58]A. B. Putranto, "Influence of a wall-embedded phononic crystal on Tollmien–Schlichting waves," Master's thesis (Delft University of Technology, 2021).
[59]M. Hussein, A. Kianfar, A. Harris, and D. Roca, "Passive flow control by metamaterial-based phononic subsurfaces," in *76th Annual Meeting of the Division of Fluid Dynamics* (APS, 2023).